Full length article

Modeling the interface structure of type II twin boundary in B19′ NiTi from an atomistic and topological standpoint

Ahmed Sameer Khan Mohammed, Huseyin Sehitoglu*

Department of Mechanical Science and Engineering, University of Illinois at Urbana-Champaign, 1206W. Green St., Urbana, IL 61801, USA

ABSTRACT

This study addresses fundamental quandaries in the understanding of Type II twin interface in *B*19′ NiTi. A combined atomistic-topological approach is proposed to resolve a longstanding debate on the interface structure, affirming the hypothesis of a semi-coherent ledged geometry comprising of disconnected terraces. Atomic registry across the terrace is shown to require interface coherence strains. The twinning plane is shown to be a non-crystallographic virtual boundary separating the strained twin variants. Consequently, the issue of lattice offset arises and is addressed by an atomistic evaluation of interface energetics upon parametric variation of an offset parameter. Required atomic movements for migration of the terrace are established from a crystallographic analysis of the strained interface structure, and validated by a Molecular Statics (MS) simulation of the twin migration segment in the Generalized Planar Fault Energy (GPFE) curve. The GPFE calculation estimates a twinning partial magnitude consistent with an earlier ab initio prediction. This twinning partial serves as a "perfect" interface dislocation which, along with the coherence strain, feed into a topological model causally explaining the known irrational indices of the effective Twin Boundary (TB). A complete mechanistic picture of diffusionless TB migration is presented, the importance of which is discussed.

© 2019 Acta Materialia Inc. Published by Elsevier Ltd. All rights reserved.

1. Introduction

Twinning plays a central role in dictating mechanical response of crystalline materials, be it as a governing microstructural constituent [1–4], a mode of inelastic deformation (deformation twinning) [5,6] or as an accommodative mode in diffusionless martensitic phase transformations (transformation twinning) [7–9]. The proposed study is most pertinent to the latter role where twinning provides a mode of Lattice Invariant Deformation (LID). This allows an energetically feasible accommodation of high distortions in transforming the parent austenite phase to the martensite phase. The impetus for this narrowed focus derives from the importance of such phase transformations in Shape Memory Alloys (SMAs) which are technologically important functional materials applied in biomedical (stents, orthodontics), automotive (valves) and aerospace fields [10]. Thermo-mechanical behavior of SMAs is significantly influenced by the mechanism of formation and migration (detwinning) of these transformation twin interfaces [11–14]. In the following study, equiatomic NiTi is chosen as the model shape memory material owing to its commercial success [15,16]. A major twinning mode in martensitic transformations in NiTi is

termed the ⟨011⟩ type II-1 twinning mode (often shortened to just type II) [16-21]. The orientation relationship between the variants is found to be a 180° rotation about⟨011⟩. It is implied (here and henceforth) that the indices are referenced to the martensite crystallographic axes. After being identified experimentally [22], these twins were characterized through the classical theory of deformation twinning [23].

1.1. Classical theory of deformation twinning

The classical theory serves as a foundation for understanding twinning crystallography, and provides a rigorous mathematical approach to translate experimentally determined orientation relationships (deduced typically from diffraction methods) to fundamental crystallographic twinning parameters (atomic planes and directions). Under the key presumption that a deformation twin is formed by a homogeneous shear of the parent lattice to twinned positions, required atomic movements (shear and shuffle) can be derived. Even now, this theory is an authoritative guide to understand atomic structure around the TB [24–26]. There are five basic twinning elements needed to describe twinning crystallography. The twinning elements comprise the invariant twinning plane K_1, twinning direction η_1, the second undistorted conjugate plane K_2, the conjugate twinning direction η_2 and the magnitude of the twinning shear *S*. These elements are derived starting from

Table 1
Twinning elements for Type II twins in NiTi, determined using the classical theory of deformation twinning (directions and planes referenced to crystallographic axes of one of the twin variants) [22].

K_1	$(0.7205\,1\,\bar{1})$
η_1	$[011]$
K_2	(011)
η_2	$[1\,0.636\quad \overline{0.636}]$
s	0.280

a known orientation relationship between the twin variants. On the basis of these orientation relationships, the theory establishes three twinning modes [23]:

(a) Type I: The twin variant lattices are related by a reflection. This reflection can either be in K_1 or in the plane normal to η_1. The elements (K_1, η_2) are rational while the others are irrational

(b) Type II: The twin variant lattices are related by a 180° rotation. The rotation can either be about η_1 or about the normal to K_1. The elements (K_1, η_2) are rational while the others are irrational

(c) Compound: The twin variants follow both Type I and Type II relationships and all twinning elements are rational

The twinning mode of interest in this study falls under the Type II orientation relationship, hence its designation. The twinning elements are tabulated in Table 1. The plane K_1 is the invariant plane under twinning deformation, whose indices are found to be irrational.

Given that the predicted twinning plane is irrational, some 10° away from $(11\bar{1})$, it is non-crystallographic in nature. The classical theory by itself cannot sufficiently explain the complete atomic structure of such an interface. Furthermore, it cannot (a) characterize the mechanism of physical growth/propagation of the twin, (b) clarify possible involvement of twinning partials in the mechanism or (c) shed light on energy-based factors that determine nucleation/propagation of the twinning modes. Addressing such aspects is neither the purpose nor within scope of these theories and they are intended primarily for a rigorous characterization of admissible twinning modes in any crystalline material. For a more detailed discussion, the reader is referred to comprehensive reviews [5,6].

1.2. Importance of a physical understanding of twin interface structure

An understanding from a classical standpoint has long sufficed the Phenomenological Theory of Martensite Crystallography (PTMC) in explaining the crystallography of the transformation [27,28]. It has also extended to the constitutive modelling of shape memory alloys [29,30]. On the flipside, a physical understanding of the irrationality of the twin interface garnered relatively limited attention. There are several reasons why such an understanding is crucial. For one, knowledge of the interface structure allows conception of nucleation and growth mechanisms for the twin on an atomic scale [31]. These mechanisms can extend to *ab initio* predictions of critical twin nucleation and propagation stresses [32,33], thereby determining the ease of activation of different twinning modes under mechanical or even thermal loads. These predictive models reveal dependencies on key physical parameters of the material, such as the stacking fault energy [6]. Such parameters can possibly be tailored by materials processing methods to engineer superior thermo-mechanical behaviors [34]. Secondly, the TB structure may hold the key to understanding functional fatigue in SMAs [35–37]. This is particularly significant for NiTi whose applications typically involve fatigue conditions [38]. A consistent agreement

has been shown between fatigue-activated slip systems in the austenite phase and the internal twinning system of the martensite phase [39,40]. An understanding of the structure is an important precursor to model possible dislocation mechanisms that can explain such fatigue-activated slip. Such a dislocation mechanism has been hypothesized in [41,42]. On a similar note, a structural understanding of the type II twin interface is vital for the magnetomechanical behavior of NiMnGa [43] (specifically to model TB mobility during the phenomenon of Magnetically Induced Reorientation or MIR [44]) which is often considered the most attractive ferromagnetic SMA [9]. The significance of such understanding cannot be overstated as type II twin interfaces find presence in other SMAs such as CuAlNi [45-47], CuZnAl [48] and AuCd [49].

1.3. Interpretation of type II twin plane irrationality: HRTEM studies

In addition to limited endeavors in this direction, there is added complexity due to controversial propositions in understanding the structure. There are dominantly two schools of thought, both of which approach the structure by observation under High-Resolution Transmission Electron Microscopy (HRTEM). An absence of consensus in the interpretation of available HRTEM images has led to a dichotomy in the understanding of the type II twin interface. While one group of researchers propose a ledged/terraced geometry with the nearest low-index rational plane {111} constituting each terrace [21,50–53], another group of researchers claim the interface to be randomly curved possessing no such features [17,18,54–56] (further extending it for type II interfaces in TiPd and NiMnGa systems, apart from NiTi). In addition, a disagreement in the irrational indices of the effective twinning plane has also been claimed [21], further adding to the perplexity in understanding the interface structure. There could be several reasons for these discrepancies. For example, slight deviations around the [011] zone axis of observation can involve effects of projectional geometry and hinder resolvability of the terraces [50]. Thus, HRTEM studies on such type II twins is a challenge and poses open problems for research.

1.4. Interpretation of type II twin plane irrationality: Topological Models (TM)

Another approach was spurred by the advent of topological modeling [57] renewing interest in the physical understanding of such irrationally-indexed interfaces [58,59]. This method relies on characterization of admissible defects on crystalline interfaces on the basis of mathematically abstracted crystallographic symmetry operations [60]. It formalizes classical theorizations of interfaces with varying degrees of coherence [61]. The classical understanding of a disconnection, prevalent particularly in context of heterogeneous twin growth mechanisms [62,63], was also formalized within the Topological Model (TM) [57]. Geometrically, the disconnection is a step-like feature separating parallel coherent terraces that are not on the same plane. These coherent terraces are crystallographic planes with rational indices. The dislocation and step character at the interface was combined within the umbrella term of a "transformation dislocation" for hetero-phase interfaces and "twinning dislocation" for the homo-phase twin interface [64,65]. The "transformation dislocation" in particular served as a useful entity in modeling interfaces of diffusionless phase transformations. One of the successes of TM was in explaining the structure of habit-planes in martensitic transformations [66–68], consistently reproducing its irrational indices so far predicted only using the PTMC [69]. Consequently, this approach was applied to the type II interface very recently by the same authors who pioneered the field [70,71]. However, in applying the model to the

Type II interface, the authors cite difficulties in theorizing disconnections for an irrational interface. Instead, their approach hypothesizes close-spaced transformation dislocations on the conjugate plane $K_2 = (011)$. To the merit of this approach, the twinning elements are well-reproduced. Yet, it is acknowledged that the final microstructure of the type II interface is still unknown. Further, there is a challenge in reconciling this model with the experimentally deduced {111}-terrace model [50,52].

Similarly, contrasting propositions have also been put forth for the mechanism by which the TB migrates. One of the proponents of the stepped geometry [52] proposed a coordinated homogeneous shear of one variant allowing a progression of the coherent terraces normal to the interface. As one of the first propositions tied with a physical interface model, this mechanism is analogous to the earliest propositions of "homogeneous" twin growth mechanism involving coordinated shear of atoms along the twinning direction η_1. However, it is now well-accepted that such mechanisms are energetically unfavorable as compared to dislocation-mediated "heterogeneous" mechanisms [6,72,73]. This is affirmed by experimental measurements of the detwinning stress in NiTi $B19'$ martensite [33,74] found to be under 100 MPa. If the mechanism was homogeneous, a detwinning stress of the same order as the martensitic shear moduli ~ 50 GPa [75] would be expected. Although the TM provides for such dislocations and outlines a heterogeneous growth mechanism for the twin, it is suggested that the disconnections cannot advance the same way as for the rational type I twin. Also, it is acknowledged that an understanding of the complete micro-mechanism of twin migration is still absent [71].

Although the aforementioned approaches seem to be at odds with each other, each offers propositions that are significant breakthroughs supporting the ensuing study. The tussle between the approaches may be resolved at two fronts. First, the elaborate atomic structural details of the HRTEM model should be reconciled within the TM framework. Secondly, the growth mechanism from the TM can be interpreted on a fundamental atomic scale for the HRTEM interface model to explain the mechanism of detwinning in a consistent manner. The proposed study attempts to reach this exact consensus, providing a bridge via atomic-scale simulations.

1.5. Overview of current approach

Atomistic simulation tools such as Molecular Dynamics (MD) [76] and Density Functional Theory (DFT) [77] have offered a probe for atomic structures at scales beyond reach of experimental techniques. They have already been employed in context of Type II interfaces [20,78], in different capacities. For the current study, these tools present a favorable environment to directly explore the nature of the type II interface on an atomic level. The methodology of this study is briefly presented here. The focus is to show the key role played by atomistic simulations. Following the propositions of the {111}-terrace model, the conditions for crystallographic coherence are explored on the terrace plane. It is shown that a certain lattice offset parameter must be determined to complete the atomic model of the terrace provided in [52]. It immediately becomes apparent that an evaluation of atomistic potential energy at various offsets is required to determine the parameter value that minimizes the energy. This evaluation would have otherwise been inaccessible in the absence of such tools. Further, if a step/disconnection is to be accommodated on the TB, there is a need to check for degeneracy in the interface energy of consecutive terrace planes separated by a step. This can be evaluated through a simulation of an atomistic twinning energy signature called the Generalized Planar Fault Energy (GPFE) [79], particularly its twin migration segment. The disconnection step height is not a topological property (in the sense, it cannot be derived solely from topological arguments) and serves as a key input parameter for the TM [57]. Furthermore, this calculation establishes the mechanism of detwinning that must be operative for migration of the TB, and also provides a magnitude for the twinning partial. The twin partial and step height are combined within a TM framework to eventually complete the type II interface model, causally explaining the irrational indices of the twinning plane. In summary, the proposed study attempts a concerted exploration of the structure of the $\langle 011 \rangle$ type II twin interface in $B19'$ NiTi through a combination of atomistic and topological modeling.

2. Modeling methodology and results

In this section, the atomistic and topological modeling approaches are presented in concurrence with their results. The purpose is to present sequential stages of a coordinated approach where the results of one step provide vital information for the methodology of the next. This is done to avoid any break in following the logical flow of the arguments. The atomistic simulations are performed in LAMMPS [76] with a governing empirical interatomic potential, solely working with energy minimization routines within a Molecular Statics (MS) framework. This tool was chosen over DFT [77] with the foresight that the resulting atomic model sets the foundation to simulate candidate dislocation-mechanisms on the TB explaining fatigue-activated slip [41,42] (refer Section 1.2). Such a simulation requires a fairly large atomic system and will incur an impractically high computational cost with DFT. Moreover, the following study does not require high accuracy in reproducing accurate potential energies of atomic interaction. Instead it only requires the interatomic potential to be capable enough to quantify, in a relative sense, the peaks and valleys of the potential energy landscape for different atomic configurations. It will be shown that this is sufficient to adequately clarify structural and mechanistic aspects relevant in this study. It is fortunate that the commercial importance of NiTi has sparked development of many state-of-the-art interatomic potentials proven to show good physical fidelity in different applications [80–82]. The interatomic potential [82] was chosen for this study.

2.1. Twin boundary crystallography

The lattice spacing and monoclinic angle in the $B19'$ unit cell are chosen following [82], consistent with the interatomic potential. The unit cell has 4 atoms, which for equiatomic NiTi are two Ti and two Ni atoms. A commonly adopted crystal description [16,83] is chosen where one of the Ti atoms is positioned at the lattice point (0, 0, 0) of the unit cell. This Ti atom is termed a lattice Ti, while the other Ti atom of the monoclinic cell is termed as a motif Ti. This is shown in Fig. 1(i). This labelling of lattice and motif atomic sites will serve a vital role in understanding atomic shuffles subsequently. These shuffles will prove important in the description of the detwinning mechanism and hence it is necessary to pay attention to the coloring schema and the labeling. Note that no distinction is made between the Ni atoms. Their behavior (in terms of relative shuffle movements) is adequately typified by the behavior of the Ti atoms and hence a further distinction would be an unnecessary complexity. The orientation relationship between the martensitic variants on either side of the TB have long been known [22]. The twinning plane, and the corresponding crystallographic system for both variants are explained in Fig. 1(ii). Here and henceforth, the variant on the top will be labeled variant A and the bottom is variant B. Under the Type II twinning relationship, the crystallographic planes $(\overline{1}\overline{1}1)_A$ and $(11\overline{1})_B$ are parallel (and hence so are their normals). The following details are important to note:

a. Within each variant, no pair of the given crystallographic directions (those indicated in Fig. 1(ii)) are orthogonal. For
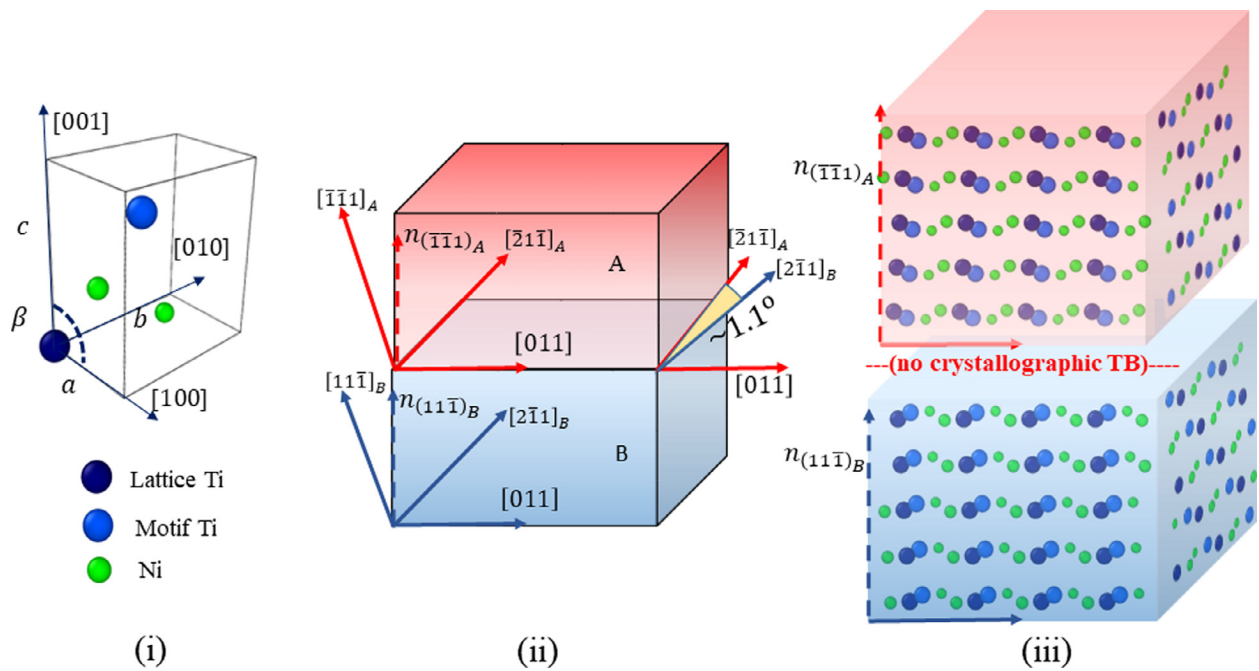
Fig. 1. (i) Designation of atomic sites in $B19'$ (ii) Crystallography of the TB (iii) Projected views of twin variants on two orthogonal planes, illustrating absence of a crystallographic twin plane (also refer Appendix B); note that this figure shows a notional positioning of the two variant blocks constructed independently (details of constructing this structure are elaborated in Appendix C) and should not be mistaken for the final twin atomic structure; complete specification of the final twin structure requires a calculation of lattice offset between the variants, as explained in Section 2.2.

instance, in variant A, no pair of directions in the set $\{[011],[\bar{2}1\bar{1}]_A,[\bar{1}\bar{1}1]_A\}$ are orthogonal to each other

b. Comparing the planes $(\bar{1}\bar{1}1)_A$ and $(11\bar{1})_B$ in variants A and B respectively, if the [011] directions of both are aligned, the directions $[\bar{2}1\bar{1}]_A$ and $[2\bar{1}1]_B$ do not align (Fig. 1(ii)). They form an acute angle, which for the chosen set of lattice constants, can be calculated as $\approx 1.12°$ (refer Appendix A). It must be mentioned that this result will change if either *ab initio* [84] or experimental lattice parameters [85] are utilized. Nevertheless, this angle is always non-zero. We choose to follow the lattice parameters of [82] for consistency with the interatomic potential.

c. The periodic spacing of the lattice points in each of these directions is the same for both the variants

In summary, there is an in-plane shear mismatch of $\approx 1.92\%$ at the twinning plane but no normal strain mismatch. This implies that there can be no atomic registry across the plane unless there is an interface shear strain applied to both the variants. Equal and opposite shear strains are applied to both variants since both are of the same phase (the TB is a homo-phase interface), and obey certain symmetry. It must be mentioned that for a general hetero-phase interface, the strain partitioning need not be equal [86]. The strain is applied following the Cauchy-Born assumption. The strain magnitude comes out to be $\approx 0.96\%$, a high value well beyond practically measured engineering elastic strains.

2.2. Relative positioning of twin variants across the boundary: lattice offset parameter

Most metallic structures possess high enough symmetry that the twinning modes exhibited are mostly of compound type [22]. In fact, *only* compound twinning is possible in the cubic lattice [87]. In such cases, the first four twinning elements of Table 1 are rational [23] and the TB separating the variants is a crystallographic plane hosting atomic sites of the crystal. This is because that plane adheres to the atomic configuration of both the twin

variants. However, from the crystallography of the {111} planes in both variants (Fig. 1(iii)), it becomes clear that there is no crystallographic plane of atoms that can match both arrangements. The reader is referred to Appendix C for a detailed account of how the TB structure can be constructed within the framework of LAMMPS. Two-dimensional projections of the complicated three-dimensional structure on the {211} and {011} planes are shown in Fig. 1 (iii) to illustrate the absence of such a crystallographic plane. A more detailed illustration is given in Appendix B. Visually, this is easy to see because of the unique arrangement of motif atoms around the lattice sites, in each variant. Hence, the TB here refers to a virtual plane separating the twin variants. While this may seem to be a detail of no importance, it immediately poses the question: What is the relative positioning of variants across the TB? This is equivalent to a formalism within the TM [59] wherein an offset vector $\vec{p}$ is defined between the variant lattices on a coincident plane. Two atomic planes are defined here to illustrate the offset coordinates. The crystallographic plane in variant A immediate to the TB is labelled $\mathbb{P}_A$ and an additional plane $\mathbb{P}_B$ of variant B is presumed to extend beyond the TB into variant A. The plane $\mathbb{P}_B$ only serves as a virtual construct to define the offsets and does not exist as a real plane in the twinned configuration. The offsets are defined by examining coincidence between the two planes. Select origins O_A and O_B on two arbitrarily chosen lattice sites on $\mathbb{P}_A$ and $\mathbb{P}_B$ respectively. The relative position of O_A with respect to O_B defines the offset vector, having coordinates (x_0, y_0, z_0). This is illustrated in Fig. 2. When all three components are zero, the lattice sites of plane $\mathbb{P}_A$ and $\mathbb{P}_B$ coincide. Of course, the offsets (x_0, y_0, z_0) exhibit periodicity corresponding to the periodic spacing along $([011], \langle 211 \rangle, \langle 111 \rangle)$ respectively and hence we narrow focus to values within the constraints $(0 \leq x_0/|[011]| < 1, 0 \leq y_0/|\langle 211 \rangle| < 1, 0 \leq z_0/|\langle 111 \rangle| < 1)$. The offsets will henceforth be represented by the normalized counterparts $(\bar{x}_0 = x_0/|[011]|, \bar{y}_0 = y_0/|\langle 211 \rangle|, \bar{z}_0 = z_0/|\langle 111 \rangle|)$.

At any offset value, the structural relationship between the two, as established by diffraction techniques (like electron diffraction in the TEM), wouldn't be any different. Hence, the foundational TEM studies that established the orientation relationship [22] could not
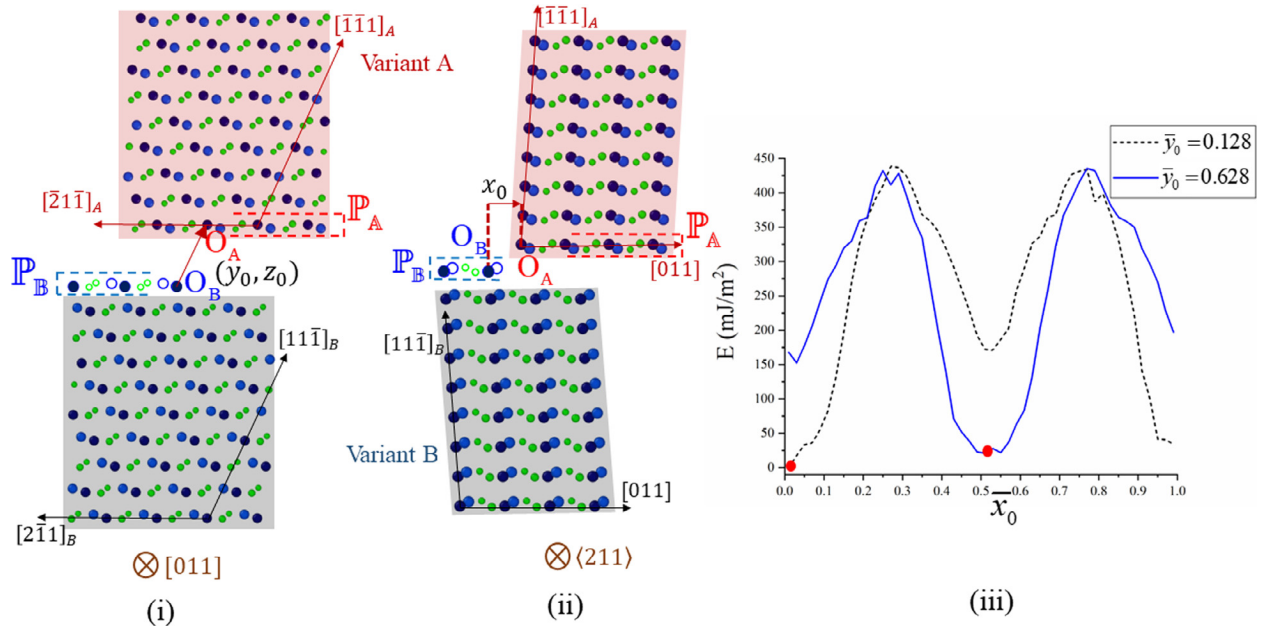
Fig. 2. Completion of TB geometry through a MS simulation to determine offsets (x_0, y_0, z_0 represent translational offsets of variant A with respect to variant B) (i) Illustrating (y_0, z_0) offsets on the (011) plane between the lattice origins O_A, O_B, on respective reference planes $\mathbb{P}_A$, $\mathbb{P}_B$ (ii) Illustrating x_0 offset on the {211}plane (iii) MS simulation results indicating offset magnitudes corresponding to minimum energy.

have clarified this detail. This issue of lattice offset is not particularly an alien concept in the context of crystalline interfaces. Offsets feature in the geometry of the "isosceles" twin boundaries [6,88] and other hetero-phase boundaries [89] as well. In fact, atomistic simulations employing static relaxation techniques were utilized to determine the structure of the "isosceles" TB in BCC structures [6].

The TEM-inspired atomic model proposed by [52] provides key insights to partially solve the problem. From their high-resolution imaging of the TB, they show that both variants appear identical when viewed along [011]. This fixes the offsets in the $\langle 211 \rangle - \langle 111 \rangle$ plane. The offset normal to the TB takes a unique value $\bar{z}_0 = 0.048$, while there are two possibilities for $\bar{y}_0 = 0.128, 0.628$ (i.e. for both $\bar{y}_0$, the variants appear identical when viewed along [011]). The relative position along [011] is not directly apparent from the atomic model. An atomistic calculation similar to that performed for isosceles twins in BCC crystals [88] is carried out here. We perform an iterative energy minimization to determine the offset $\bar{x}_0$ through molecular statics, and this is performed for each value of $\bar{y}_0$. By initiating the statics relaxation from various atomic configurations distinguishable by $\bar{x}_0$ offset, the offset value corresponding to the least energy is identified. After enforcing the coherence strain, the axes of the simulation box align as follows: $x \| [011]$, $y \| [\bar{2}1\bar{1}]_A$, $z \| n_{\{111\}}$. The lateral axes, x and y are crystallographic, implying that periodic conditions can be setup to represent the bulk material, while the boundary parallel to the TB is shrink-wrapped. For the box size, a span of 10 periodic spacings along [011] (one periodic spacing ~ 6.36 Å) and $\langle 211 \rangle$ (one periodic spacing ~ 8.29 Å) is chosen, and 30 {111} planes chosen along z direction (spacing between consecutive planes ~ 2.097 Å). Assuming that the structure far from the twin interface remains unaffected in this iterative relaxation procedure, a 6 Å boundary is constrained or "frozen" on the top and bottom. The relative positions of atoms in these layers are constrained to remain unaffected by the forces enforced by the energy minimization routine. The thickness was chosen to be higher than the cutoff distance of the interatomic potential ($r_c = 5.2$ Å). The conjugate gradient relaxation scheme in LAMMPS is employed where convergence is said

to be achieved when the fractional energy change over successive iterations is less than 1.0×10^{-8}. During the relaxation, the dimensions of the simulation box is allowed to vary using the box/relax option, thus allowing a dilatational relaxation to the TB aiding it in achieving the lowest energy configuration for each offset. The parametric variation of the offset is achieved by changing an "origin" parameter (a provision in LAMMPS when defining lattices) within the code. The result are the values of the offset parameters $(\bar{x}_0, \bar{y}_0, \bar{z}_0) = (0.522, 0.128, 0.048)$ or $(0.022, 0.628, 0.048)$. Both these offsets are crystallographically equivalent in that they correspond to the same resulting TB structure. This completes the atomic model of the coherent twin segments proposed by [52], for the Type II TB in $B19'$ NiTi martensite. The plot in Fig. 2(iii) presents the relative energies with reference to the lowest energy configuration. The absolute value of this minimum energy reflects the twin boundary energy (more generally it is the grain boundary energy, estimated from atomistics following [90]) for the {111} terrace plane. An alternate choice of the terrace plane, such as {344}, yields a higher twin boundary energy. Moreover, it does not relax as well as the {111} interface, producing significant local distortions around the twin boundary. This justifies the choice of terrace plane as {111}.

2.3. Atomic shuffles transforming one twin variant to another

Now that the crystallography of the TB has been established, the atomic motions necessary for detwinning are determined. For this purpose, two twinned configurations T1 and T2 are compared that differ by the existence of one additional detwinned layer plane in T2. It must be pointed that the setup of both these configurations is now conceivable only after due completion of previous offset calculation. The crystallographic arrangement in $(11\bar{1})_B$ plane of variant B in T1 is compared against the corresponding detwinned $(\bar{1}\bar{1}1)_A$ plane in variant A of T2 (Fig. 3). Sub-regions of the corresponding planes are overlapped to aid the visualization of the atomic movements. The following observations are made:

a. The entirety of atomic movements has a negligible average translational component and dominantly comprises shuffling
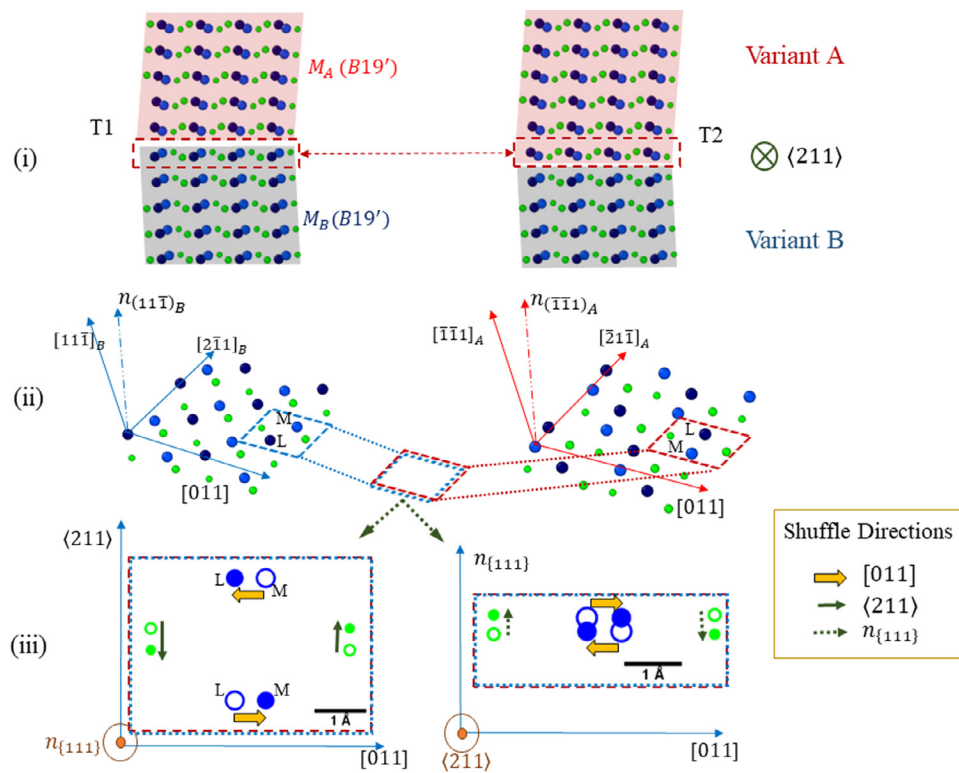
Fig. 3. (i) Atomic arrangement of twin as viewed along ⟨211⟩, highlighting the crystallographic plane which detwins from a variant B configuration in T1 to a variant A configuration in T2 (ii) Comparison of atomic arrangement on the plane undergoing detwinning (iii) Overlapped atomic positions indicating necessary atomic shuffles for detwinning (filled circles correspond to atom positions in variant A while open circles correspond to variant B; L: Lattice Ti, M: Motif Ti), achieving the conversion of the crystallographic plane in variant B to a plane in variant A.

movements around the TB. These are the shuffles that must be realized for migrating the TB.

b. The lattice Ti site (L) of variant B must move to the motif site (M) in variant A of T2. Similarly, the motif Ti of variant B (T1) are to move to the lattice Ti sites in variant B (Fig. 3(iii)). These movements are along [011] only.

c. As for the Ni atoms, an equal and opposite movement along ⟨211⟩ and $n_{\{111\}}$ is required

This analysis was done in expectation of the GPFE calculation elaborated in the next section. Knowledge of these atomic movements is necessary to simulate the detwinning within the MS framework under the right constraints.

2.4. Twin migration segment of the GPFE curve

Following the previous section's analysis, if the detwinning dominantly requires shuffles at the TB, then it can be asked what role is played by the twinning shear s (Table 1)? How does an applied shear on the TB connect with the shuffles required to migrate the same? An atomistic simulation of the GPFE curve is ideal to elaborate this shear-shuffle interplay, and will be calculated in this section. It would be unreasonable to expect the exact energy landscape because the MS framework is not truly ab-initio. It relies on an empirical interatomic potential that was not fit to any energy signature corresponding to twinning. An *ab initio* calculation of the GPFE landscape is given in [20]. In particular, we will focus on the twin migration segment of the GPFE curve and ignore the nucleation segment. The reader is referred to [79] for details on the procedure to obtain the GPFE curve, and also to Appendix D where certain specifics in the applicability of the procedure to this low-symmetry phase is discussed. In short, the standard procedure attempts to incrementally introduce a rigid translational disregistry

between the two variants at the TB and tracks the energy cost for the same. This is typically done by rigidly displacing one variant (mobile half of the system) on top of the other (fixed half of the system) until the TB has migrated to the next plane. The translational disregistry plays the role of the twinning shear and following [20], it is known to be along [011]. This causes a TB migration into variant B, causing one layer plane of variant B to detwin into variant A.

Following these guidelines, a MS simulation is setup. The twin configuration T1 (Section 2.3) is setup with periodic lateral conditions and shrink-wrapped conditions on the top and bottom. The constrained layers with thickness higher than the potential cut-off are set at the top and bottom, following Section 2.2. The mobile half of the system is defined as variant A along with an additional atomic plane of variant B which is about to detwin. The remaining portion of the system is the fixed half. In the mobile half of the system, the lattice Ti sites are constrained to follow incremental rigid displacements along [011], while in the other half they are constrained to stay fixed (Fig. 4). With the lattice Ti constrained, the motif Ti atoms and the Ni atoms are allowed to relax about their positions without any constraint in any direction. An additional out-of-plane shuffle is also allowed for the lattice Ti atoms. Explaining the rationale behind this procedure requires a digression that is not directly pertinent to the main study and is hence deferred to Appendix D. At every increment of rigid displacement, an energy minimization is carried out with the conjugate gradient method in LAMMPS, until energy converges to within a fractional change of 1.0×10^{-8}. The volume of the simulation box is maintained constant throughout. The results are presented in Fig. 4. A steep drop is obtained at the onset of the lattice-motif Ti shuffle. Different points of the obtained GPFE curve are corresponded with snapshots of the intermediate structural states at that position.
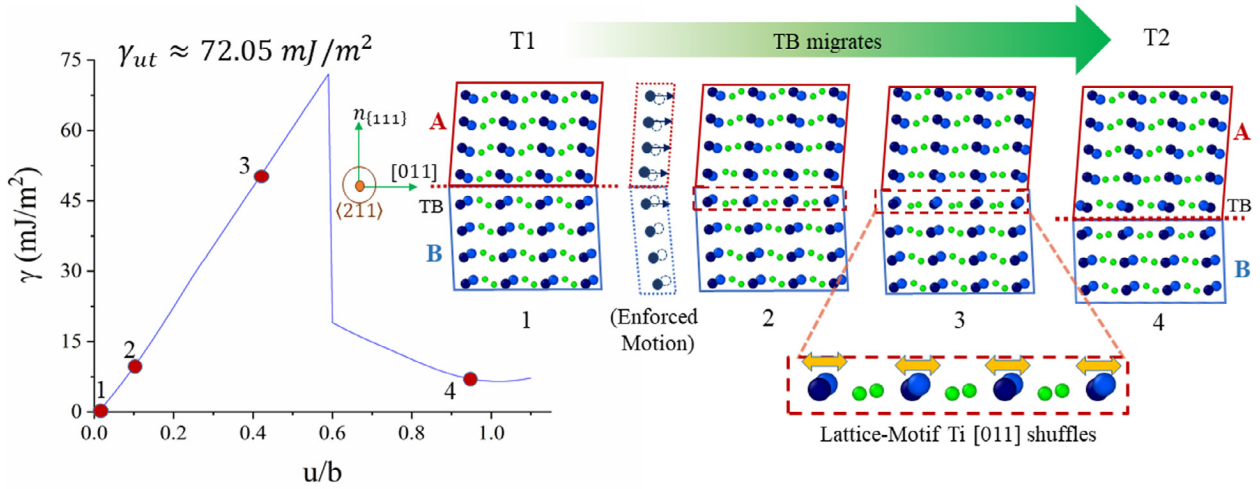
Fig. 4. GPFE curve from Molecular Statics: The enforced rigid motion on the lattice Ti sites(u||[011]) is schematically indicated, and snapshots of atomic positions at different stages is presented.

Although only the Ti shuffles have been illustrated in the figure, the Ni shuffles also happen simultaneously.

We focus on two takeaways for the final modeling step. Note that the potential energy after detwinning (configuration T2, at 4) nearly recovers to the initial value (configuration T1, at 1). This reflects the periodicity of the twin migration segment in the GPFE curve and this periodicity corresponds to the magnitude of the twinning partial [79,91]. The "partial" nature is associated with the property of the dislocation in migrating the generalized planar fault that is the twin boundary (TB). The magnitude is only slightly lower than that proposed in [20] i.e. $b \approx 1/9[011]$, and was used as a scaling factor for the displacement axis in the plot in Fig. 4. The TB has migrated by one plane and the TB energy is degenerate before and after migration. Both aspects are relevant to the TM derived in the following section, and a discussion on the shear-shuffle interplay is deferred to the discussions section.

2.5. Disconnected geometry of ⟨011⟩ type II twin boundary: Topological Modeling (TM)

The ensuing section attempts to causally explain the observed disconnected geometry of the TB observed in [21]. In Section 2.1 it was established that there is an interface shear strain needed to have perfect atomic registry across the TB. To minimize the elastic strain energy cost associated with the TB, long-range strains must be minimized by an array of dislocations at the interface rendering it semi-coherent [61]. Further, the twin interface also accommodates disconnections [21,50], which from TM are responsible for the diffusionless migration of the twin interface [73]. Such a dislocation-disconnection combination is directly embodied in the twinning partial calculated in the previous section. The presence of a twinning dislocation on the interface separates two coherent {111} terrace planes by a step/disconnection [6,62,64]. Given the degeneracy in energy for the TB residing on successive planes (Section 2.4), the disconnection can step between consecutive {111} terraces separated by one interplanar spacing i.e. $d_{\{111\}} \sim 2.097$ Å. Then the twinning partial is a "perfect" interface dislocation, following terminology of [64]. This step height in combination with the magnitude $|b| \approx 1/9$ |[011]| are key parameters for the TM. The iterative approach described in [67] is utilized. For the first iteration, the twinning plane indices are assumed as $n_0 = (11\bar{1})_B$, and the axes are chosen with the x axis aligned along the common [011] direction, y along ⟨211⟩ and the z axis pointing into variant A, aligned with $n_{(11\bar{1})_B}$ (refer Fig. 5). The linear density of interfa-

cial defects (dislocations), **B**, is given by Frank-Bilby equation, expressed here in the tensorial form:

$$\mathbf{B} = -\mathbf{E}_c.\mathbf{v} = -(\mathbf{D}_A^{-1} - \mathbf{D}_B^{-1}).\mathbf{v} \tag{1}$$

Where $\mathbf{E}_c$ is the interface coherence strain and **v** is a unit probe vector along which the linear density is sought, and $\mathbf{D}_{A(\text{or}B)}^{-1}$ is the deformation gradient tensor that maps the strained state in the twin configuration to the un-deformed crystallography of the individual variant A (or B). The magnitude of the coherence shear strain in each variant is given by $\gamma = 0.96\%$. The individual deformation gradients are given by:

$$\mathbf{D}_A^{-1} = \begin{pmatrix} 1 & -\gamma & 0 \\ 0 & 1 & 0 \\ 0 & 0 & 1 \end{pmatrix}; \mathbf{D}_B^{-1} = \begin{pmatrix} 1 & \gamma & 0 \\ 0 & 1 & 0 \\ 0 & 0 & 1 \end{pmatrix} \tag{2}$$

Substituting in (1), and using the probe vector along the y-axis $[010]^T$(which is aligned with ⟨211⟩), the dislocation density is given by:

$$\frac{\mathbf{b}}{d} = \mathbf{B} = 0.0192 \tag{3}$$

The twinning partials are of screw nature with their dislocation lines and Burgers vector aligned along [011], having magnitude $b = 1/9\,[011] \approx [0.7067\,0\,0]^T$Å. Substituting in (3), we solve for the disconnection spacing, which in the first iteration is $d_0 = 36.80$Å. For this spacing, the effective normal to the twinning plane is rotated by the transformation

$$Q = \begin{pmatrix} 1 & 0 & 0 \\ 0 & \cos\theta & -\sin\theta \\ 0 & \sin\theta & \cos\theta \end{pmatrix} \tag{4}$$

where, given the inter-planar spacing of $(11\bar{1})_B$ planes as $h_{(11\bar{1})} \approx 2.097$Å, we get $\theta_0 = \tan^{-1}(h_{(11\bar{1})}/d_0)$. Thus, an inclination is introduced into the effective twinning plane which changes it slightly from $(11\bar{1})_B$. The calculation is repeated in a rotated set of axes $x' - y' - z'$ (Fig. 5), where $x'\|$ [011] and z' is along the normal to the new effective plane. Applying this rotation to the homogeneous coherence strain and repeating the calculation iteratively, a self-consistent twinning plane is determined. To show the convergence, results of 3 iterations are given in Table 2. The resulting twinning plane agrees with the HRTEM observation of [21], being closer to $(8\,9\,\bar{9})_B$ than the classical/PTMC indices of $(0.7205\,1\,\bar{1})_B$.
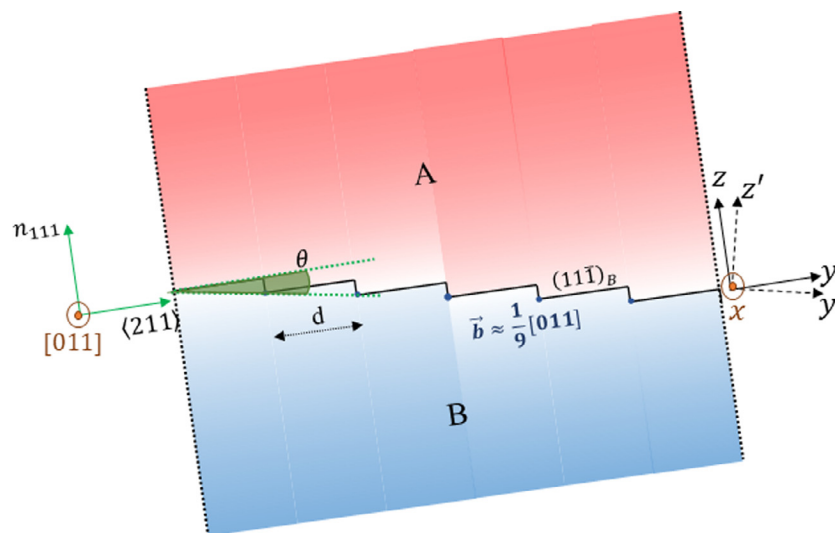
Fig. 5. Schematic for topological model parameters.

Table 2
Iterative topological model calculation of effective twinning plane for Type II system.

Iteration	Spacing of partials (Å)	Inclination (deg)	Effective Twinning plane
1	36.798	3.261	$(1\,1\,\bar{1})_B$
2	36.858	3.261	$(0.8619\,1.0229\,\overline{1.0269})_B$
3	36.858	3.261	$(0.8621\,1.0229\overline{1.0269})_B$

3. Discussions

3.1. Coherence strains for crystallographic registry

The requirement of coherence strain for atomic registry is solely due to the non-orthogonality of the crystallographic axes (Fig. 1(ii)), and does not involve any further atomic-feature as such. And as shown in Section 2.5, these coherence strains are counteracted away from the interface by the presence of an array of twinning dislocations at the interface. After multiple iterations, there is still a residual elastic strain energy corresponding to the TB. This elastic energy corresponds to a small magnitude of residual strain far away from the interface (it can't be perfectly nullified by the interface dislocations). It also includes the self-energies and interaction energies of the interface dislocations. And this is independent of the intrinsic stable twin stacking fault energy γ_{tsf} that typically governs the thermodynamics of nucleation of a given twinning mode [92].

As mentioned earlier, the root cause of the coherence strain is the non-orthogonality of the axes which can be traced down to the monoclinic distortion in the unit cell of $B19'$. This extends to a more fundamental question on the crystal structure of low-symmetry phases, particularly those of martensitic phases in SMAs: If the axes of the unit cell are further away from orthogonality, what implications does it have on the occurrence and the structure of such Type II twinning modes? From the present analysis, a first guess would be that the elastic strain energy cost would be higher. This is because closer spaced dislocations (and hence higher repulsive interaction) would be required to alleviate higher coherence strains. And the shorter spans of crystallographic terrace planes implies the effective TB has irrational indices further removed away from the rational indices of the coherent terraces. Note that the classical theory [23] does not account for the presence of such strains. The lattice vectors of the unstrained variants (which only prevail furthest from the interface) are used as an input and hence it becomes obvious that there can be no rational twinning plane K_1 in the absence of coherence strains. Note that the rationality of the shear direction $\eta_1 = [011]$ remains unaffected because this

direction is out of the plane which hosts the inclination angle θ (refer Fig. 5). Hence, the direction of twinning shear $\eta_1 = [011]$ established on the coherent {111} terrace planes (Section 2.4) directly translates to the effective irrational twinning plane as well.

3.2. Absence of crystallographic TB and lattice offsets

The unique arrangement of motif atoms in the unit cell of $B19'$ are primarily responsible for the absence of a crystallographic TB. Further supporting arguments are provided in Appendix B. It is shown there that if these motif atoms are ignored and the twin is constructed using lattice points alone, a crystallographic TB does exist hosting coincident lattice sites of both variants. As a direct consequence of the motif atoms, the twin configuration has a relative offset between the lattices. It is remarkable to note that this offset positions the variants in such a manner that a shuffle among the Ti (lattice-motif shuffle) and Ni atoms is sufficient to migrate the TB by one crystallographic plane (refer Fig. 3). Hence, to draw a fundamental connotation, although the motif units of the $B19'$ unit cell complicate the twin configuration geometry and necessitate the calculation of an offset, they attribute the unique capability of shuffling into twinned positions with relatively low energy barriers [20].

3.3. Shear-shuffle interplay

A few comments on the GPFE calculation are prudent here. The unstable twinning energy γ_{ut} is 72mJ/m², which is significantly higher than the accepted value [20]. Also, while the shuffling movements amongst Ni atoms are achieved, there are minor deviations in their final positions within the detwinned plane. This is in comparison to the T2 configuration setup in the previous section. Thirdly, the GPFE twin migration segment looks highly unsymmetric (Fig. 4), exhibiting a steep energy drop at the onset of the lattice-motif shuffles (again, does not agree with [20]). Nevertheless, these discrepancies must be borne as a limitation of the interatomic potential, which is state-of-the-art. Moreover, the motive of this calculation is significantly different than that of [20],
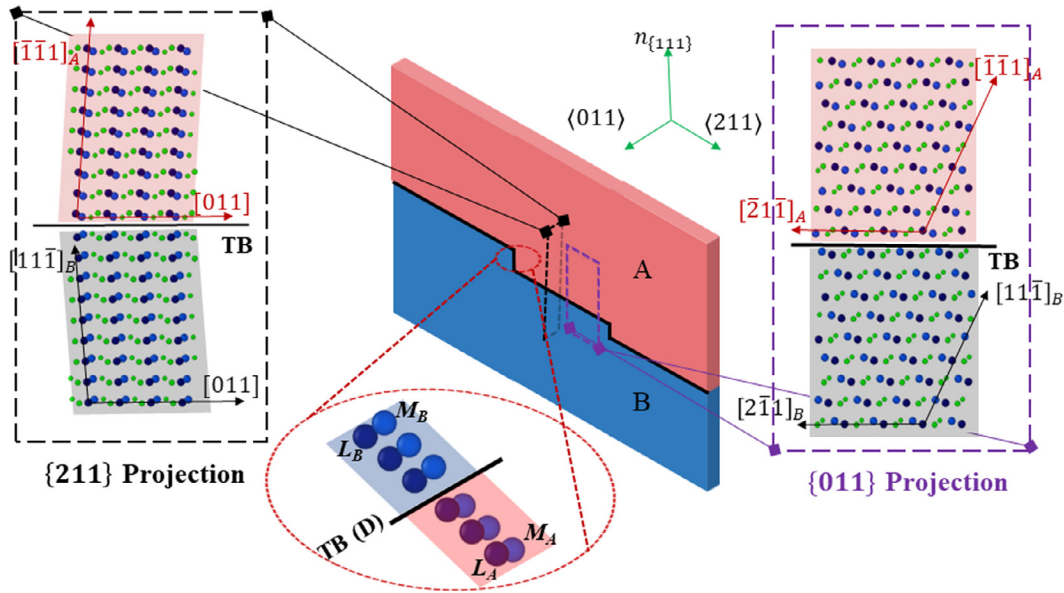
Fig. 6. The disconnected twin interface geometry is shown with projections of the atomic structure on the coherent terrace planes. The crystallography surrounding the disconnection is also schematically shown, where TB (D) represents the Twin Boundary Disconnection; L_A, M_A are the lattice and motif Ti sites in variant A respectively, and for variant B we have the analogous designations L_B and M_B.

and primarily aims at thoroughly characterizing the detwinning mechanism. For these purposes the MS simulation and the interatomic potential are sufficiently useful.

Note that the lattice-motif Ti distinction (Section 2.1) was crucial in the GPFE simulation. Selectively applying the rigid displacements to lattice sites allows us to infer a gradation in the degree of shuffle from near the interface to away from the interface. Treat the rigid displacements enforced on lattice sites equivalent to an applied shear. Further away from the interface, the motif units follow the lattice Ti and contribute to the magnitude of the twinning shear s. As we move closer to the TB, there is a higher propensity for the motif atoms to shuffle. At the TB, the entirety of atomic movements are shuffles with negligible average displacement of atoms. This is very different from the compound twinning modes in higher-symmetry cubic systems where the shear plays a more dominant role than shuffle (refer Appendix D).

3.4. Topological Model (TM) complete with atomistic twin migration mechanism

Possibly the key ingredient in applying the TM was the interface coherence strain. It causally explains the need to have a periodic array of interface dislocations which eventually explains the irrational effective twin plane. The GPFE calculation was necessary to establish a degeneracy in interface energy between consecutive {111}terrace planes. This is the additional input required by the TM to stipulate the disconnection step height [57]. In addition, it was necessary to establish the shuffles required for detwinning or TB migration.

The advantage of approaching the problem from an atomistic standpoint can now be realized where, along with the topological model the mechanism of twin migration can be fully clarified. It allows the partitioning of shears and shuffles in detwinning to the disconnection and dislocation components [73], respectively, of the interface twinning dislocation. The motion of the disconnection is accompanied by a progression of the shuffles (elaborated in Sections 2.3 and 2.4). The twinning dislocation magnitude is not as pertinent to the interface structure and has a more macroscopic implication in countering the interface coherence strains from

extending long-range. Further, it acts as a carrier of the twinning shear as it moves along with the disconnection.

A complete picture of the interface structure is provided in Fig. 6. The atomic structure around the disconnection is also shown where the Twin Boundary Disconnection, TB (D), demarcates the two variants on the same crystallographic plane. Only the Ti atoms are shown for clarity of presentation. The difference in the relative positions of Lattice (L) and motif (M) Ti's are illustrated in both variants A and B. Suffice it to say that the Ni atoms also exhibit similar distinctions. It must be mentioned here that the structure here only highlights the crystallography and has not been relaxed within MS. If it was, there would be a more gradual change in structure across the TB (D). This is an unnecessary complication for this study and is excluded. Fig. 7 highlights the lattice-motif Ti shuffles accompanying migration of the TB (D), that advances the TB. There are lattice-motif exchanges along [011] as indicated. These shuffles are consistent with the analysis in Section 2.3 and from the GPFE calculation (Section 2.4). Although not shown, the Ni atoms also exhibit shuffles following Section 2.4. As the dislocation component progresses to migrate the terraces by one crystallographic plane, the net twinning shear is $s = b/h$ [6] equaling ≈ 0.34, where the twin dislocation magnitude is $b = \frac{1}{9}|011| = 0.7067\,\text{Å}$ and the step height is $h = d_{\{111\}} = 2.097\,\text{Å}$. If, instead of the interatomic potential's lattice parameters, more accurate experimental [85] or *ab initio* lattice parameters [84] are utilized, the value improves to $s = 0.31$, close to the phenomenologically determined twinning shear (Table 1).

3.5. Reconciling the HRTEM and the TM model

In Section 1, it was mentioned that a consensus between the HRTEM model and the TM approach would be reached through atomistics. This is elaborated by noting the following two links:

a. The TM approach [71] cites difficulties in formulating disconnections on an irrational twin plane. The HRTEM-model [52] observes the effective irrationality of the plane to arise from a stepping between rational terrace planes. Having adopted the latter explanation, the key question was: Why does the twin interface prefer such a geometry over a single coherent plane? And interestingly, through the detailed
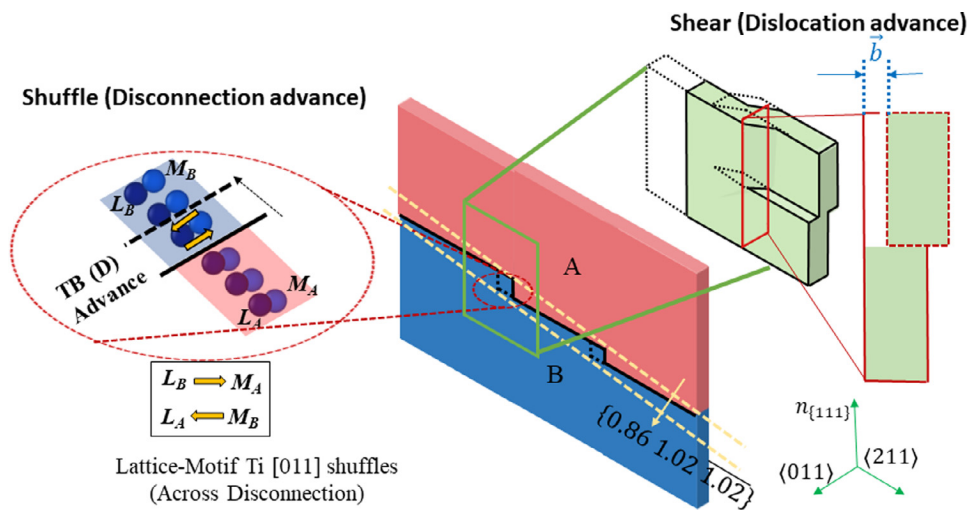
Fig. 7. The mechanism of TB migration of the effective twin interface $\{0.86 1.02 \overline{1.02}\}$ is shown; It occurs through the motion of the interface twinning dislocations comprising a dislocation component (Burgers vector $\vec{b}$ carrying the twinning shear) and a disconnection component (involving the lattice-motif shuffles for Ti atoms; although not shown here for clarity, there are also shuffles associated with Ni atoms, as per Section 2.4).

characterization of atomic registry on the rational terrace plane (Section 2.1), a coherence strain was determined. Such interface coherence strains constitute a crucial aspect of the TM theory [58,93], and the same framework immediately explains the irrational indices adhering to the disconnected geometry proposed by the HRTEM-model.

b. Although the concept and role of a disconnection in boundary migration had been formalized within TM theory, the HRTEM model identified its existence (called it "steps") on the TB independent of those findings. This could possibly be the reason why the step/disconnection was treated as a pure geometrical feature, and no significant role was attributed to it for the twin migration mechanism. The HRTEM model was blind to the idea of having dislocations on these disconnections, or blind to the idea of transformation/twinning dislocations. The dislocation component carries the twinning shear (heterogeneous mechanism) while the disconnection geometrically advances the boundary causing one twin variant to grow at the cost of the other (Fig. 7). These were basic tenets of the TM theory. Linking the two concepts required the GPFE simulation (Section 2.4) to which the lattice offset simulation is a precursor (Section 2.2).

4. Conclusions

This study attempts to provide a complete structural model of the $\langle 011 \rangle$ Type II twin boundary in $B19'$ NiTi, building on experimental HRTEM propositions [52]. A concerted modeling approach coupling atomistic simulations with TM theory is utilized to provide a physical explanation for the irrational indices of the TB. Adopting the {111}-terrace model of [52], requirements for atomic registry on the terrace plane are established. It is found that the TB cannot be crystallographic and is a virtual plane separating the variants. Also, an interface coherence strain is required for atomic registry across this boundary. The issue of lattice offset arises and is addressed using an iterative energy minimization scheme within MS, thereby determining the offset parameters that complete the terrace atomic model of [52]. Subsequently, the crystallography of the TB is analyzed to establish the necessary atomic motions for detwinning. This detwinning mechanism is simulated within a MS framework by way of calculating the twin migration segment of the GPFE curve. The interplay of shear and shuffles in migrating the TB are established. An estimate for the twinning dislocation is

obtained along with a step/disconnection height that can separate energetically degenerate {111} terraces. These are combined within a TM [58] to causally explain the irrational indices of the effective twinning plane K_1, formerly determined from classical theories [22,23]. Physical explanations for some of the classical twinning elements (K_1, η_1, s, in particular) were provided. The predicted K_1 in fact agrees better with more recent experimental findings [21] than the phenomenological characterization [22]. The role of the dislocation component in carrying the twinning shear and the shuffling mechanisms undergone during disconnection advancement are also established, thereby providing a complete description of the twin migration mechanism. The merits of the proposed approach in reconciling the HRTEM-based model within the TM theory have been outlined, highlighting the crucial insights from atomistics that bridged the hitherto disjoint propositions. In conclusion, this study attempts to provide both a complete structural model and a mechanism for twin propagation for Type II twins in $B19'$ NiTi. It attempts to fill a void in the physical understanding of this interface [71], the crucial implications of which have been discussed.

Declaration of Competing Interest

The authors declare that they have no known competing financial interests or personal relationships that could have appeared to influence the work reported in this paper.

Appendix A. Interface shear strain mismatch on the {111} coherent terraces

This section shows the calculation of the interface shear strain mismatch between the planes $(\overline{1}\overline{1}1)_A$ and $(11\overline{1})_B$ in variants A and
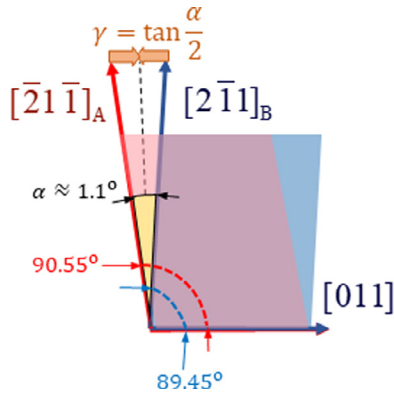
Fig. A.1. Illustration of the angular mismatch when the variant planes $(\bar{1}\bar{1}1)_A$ (red) and $(11\bar{1})_B$ (blue) are overlapped.

B respectively. First, the lattice vectors of the monoclinic unit cell are represented in an orthonormal basis $\{\hat{e}_1, \hat{e}_2, \hat{e}_3\}$. The basis is chosen such that $\hat{e}_1 \| [100]$, $\hat{e}_2 \| [010]$ and $\hat{e}_3 = \hat{e}_1 \times \hat{e}_2$. The lattice parameters are chosen consistent with the interatomic potential [82], $a = 2.699$ Å, $b = 4.386$ Å, $c = 4.606$ Å, $\beta = 93.41º$. In the orthonormal basis, the components of the lattice vectors are:

$$[100] = \begin{pmatrix} 2.699 \\ 0 \\ 0 \end{pmatrix}; [010] = \begin{pmatrix} 0 \\ 4.386 \\ 0 \end{pmatrix}; [001] = \begin{pmatrix} -0.274 \\ 0 \\ 4.598 \end{pmatrix} \quad (A.1)$$

Then we have,

$$[011] = \begin{pmatrix} -0.274 \\ 4.386 \\ 4.598 \end{pmatrix}; [\bar{2}1\bar{1}] = \begin{pmatrix} -5.124 \\ 4.386 \\ -4.598 \end{pmatrix}; [2\bar{1}1] = \begin{pmatrix} 5.124 \\ -4.386 \\ 4.598 \end{pmatrix}$$
$$(A.2)$$

Taking dot products, we can compute the angle between [011] and $[\bar{2}1\bar{1}]$ as 90.55º. The angle between [011] and $[2\bar{1}1]$ is 89.45º. Now following the crystallography specified in Section 2.1, if the variant planes $(\bar{1}\bar{1}1)_A$ and $(11\bar{1})_B$ are overlapped, the scenario represented in Fig. A.1 results.

The angular mismatch $\alpha \approx 1.1º$ is specified. An equal and opposite shear strain must be applied to both variants, calculated as $\gamma = \tan \frac{\alpha}{2}$. The net interface shear strain mismatch is $2\gamma \approx 1.92\%$

Appendix B. Non-crystallographic TB

The crystal structures of twin variants A and B of $B19'$ NiTi martensite are visualized, given in Fig. B.1. No crystallographic TB is admissible between the variants because no atomic plane adhering to the arrangement in both variants is possible. Now consider only the lattice sites (only lattice Ti) in each variant. With only the lattice points, a crystallographic TB is possible. This is because the lattice sites of both variants coincide on this plane (Fig. B.2). An atomistic computation of lattice offset (Section 2.2) is unrequited here. The relative offset (of Section 2.2) is zero and the lattice points of both variants coincide. The purpose of this exercise is to show that the absence of a crystallographic TB arises fundamentally from the presence of motif atoms within the unit cell of martensite (Fig. 1(i)). This attributes a unique crystallographic arrangement within each variant which cannot be matched to form an atomic plane for the TB.
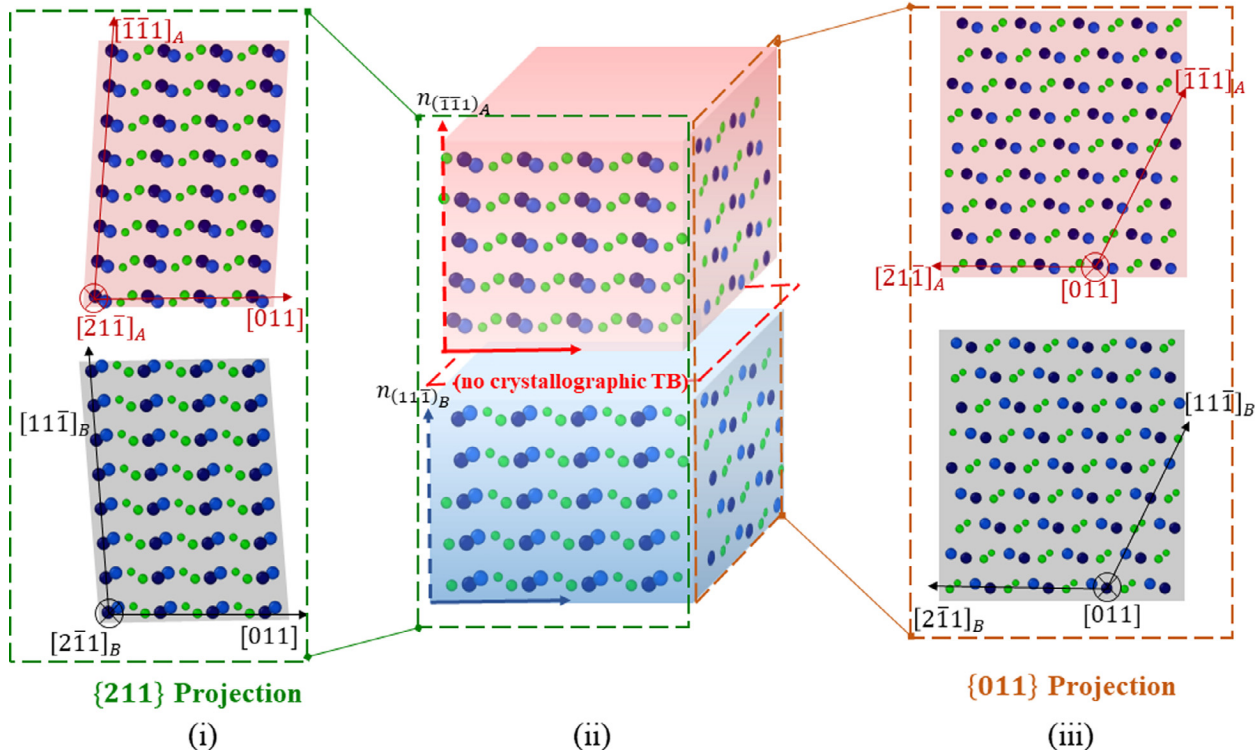

Fig. B.1. (i) {211} projection of twin variant crystal structures (ii) Combined variant projections in a three-dimensional form, indicating inadmissibility of a crystallographic TB (iii) {011} projection of twin variant crystal structures.
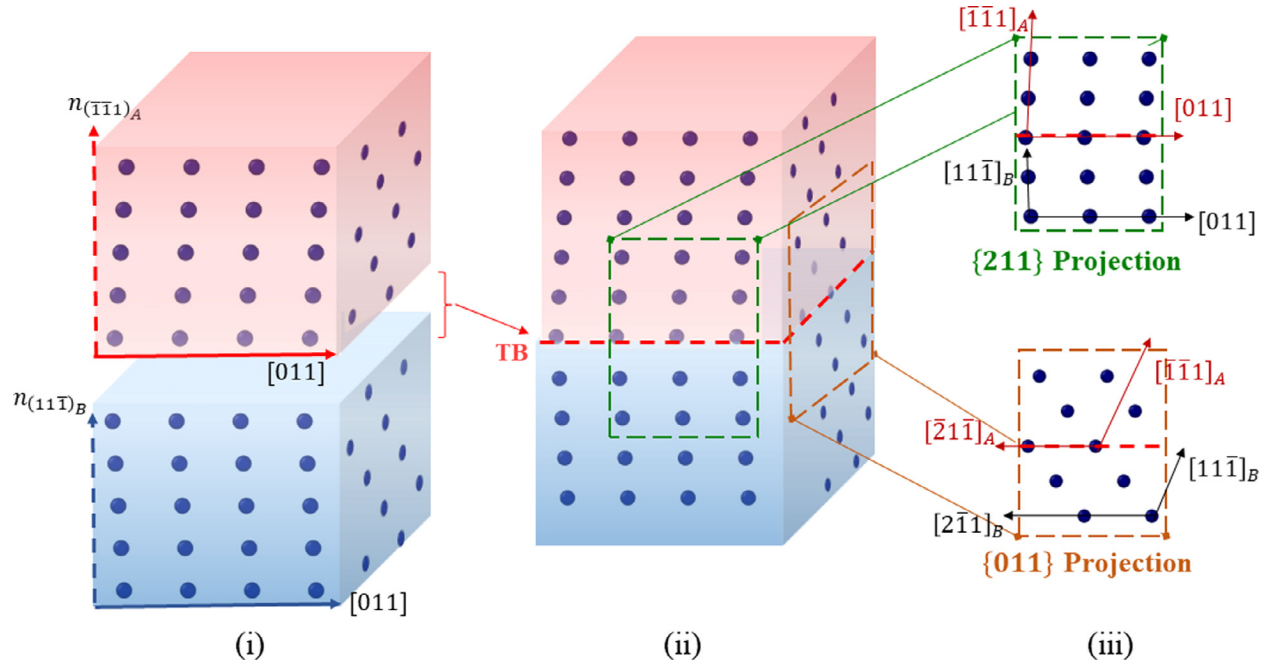
Fig. B.2. (i) Combined variant projections in a three-dimensional form, considering only lattice sites and ignoring motif atoms (ii) The lattice sites of both variants coincide on a crystallographic TB (iii) {211} and {011} projection of twin variant lattices, indicating a crystallographic TB.

Appendix C. Construction of the {111} terraces of the Type II twin boundary

This section provides a detailed account of how the atomic structure on the {111}rational terrace can be constructed within the framework of LAMMPS. We start with the dimensions and axes of the simulation cell defined in a global orthonormal system $\{\hat{i}, \hat{j}, \hat{k}\}$. The x-axis aligns with $\hat{i}$, y-axis with $\hat{j}$ and z-axis with $\hat{k}$. LAMMPS allows a definition of a simulation box in space, where the span along each axis is given by a start and end coordinate. Thus the limits on each axis are given by the pairs (x_{min}, x_{max}), (y_{min}, y_{max}) and (z_{min}, z_{max}). Additionally, the simulation box can be defined as a parallelepiped, suited for a general triclinic structure. Setting the origin of the parallelepiped at $(x_{min}, y_{min}, z_{min})$, the edge vectors are defined in the global basis by the coordinate sets: $\vec{L}_1 = (x_{max} - x_{min}, 0, 0)$, $\vec{L}_2 = (xy, y_{max} - y_{min}, 0)$ and $\vec{L}_3 = (xz, yz, z_{max} - z_{min})$. This is similar to the definitions in [94]. Next, a crystal is defined in space. This is done by indicating the unit cell lattice vectors and the basis atoms in the unit cell. The unit cell lattice vectors must be defined in the global basis depending on how the lattice is to be oriented in space. Given the lattice and the motif atoms, a crystal is generated in space. Then LAMMPS cuts-off all atoms outside the boundaries of the defined simulation box and only retains the atoms that fall within it. We illustrate this with the example of constructing a single variant, variant A, in an appropriate simulation box.

Following the crystallography of Section 2.1, we define a parallelepiped such that $\vec{L}_1 || [011]$, $\vec{L}_2 || [\bar{2}1\bar{1}]_A$ and $\vec{L}_3 || [\bar{1}\bar{1}1]$. Selecting the edges to be crystallographic directions is crucial to allow enforcement of periodic boundary conditions along them. Also the edge lengths must be an integral multiple of the periodic spacing along these directions. Otherwise, "critical-edge" effects can arise, as noted in [94]. We choose the edge lengths to be 10 periodic spacings in each of these directions. This means that $\vec{L}_1 = 10[011]$, $\vec{L}_2 = 10[\bar{2}1\bar{1}]$ and $\vec{L}_3 = 10[\bar{1}\bar{1}1]$. Also, we choose $x_{min} = 0$; $y_{min} = 0$; $z_{min} = 0$. To determine the coordinates of the edge vectors we must determine their lengths and also the angles between them. Let the angles between $\vec{L}_1$ and $\vec{L}_2$ be defined as γ, the an-

gle between $\vec{L}_2$ and $\vec{L}_3$ be α and that between $\vec{L}_1$ and $\vec{L}_3$ be β. The lengths and angles of these vectors can be computed by expressing coordinates of these crystallographic directions in a common orthonormal basis. We use the $\{\hat{e}_1, \hat{e}_2, \hat{e}_3\}$ basis defined in Appendix A, and follow that procedure to get the coordinates of $\vec{L}_i's$. In other words, the coordinates in equation (I.2) will be used. The lengths can be computed by taking norms and the angles by taking dot products. The following parameters are determined.

$$L_1 = 63.602 \, \text{Å}; L_2 = 81.629 \, \text{Å}; L_3 = 71.015 \, \text{Å}$$
$$\alpha = 116.044^\circ; \beta = 86.508^\circ; \gamma = 90.551^\circ \qquad (C.1)$$

They can be recast into the relevant coordinates to specify the simulation box. Let [011] be chosen to be aligned to the x-axis of the simulation box and the x-y plane as the $(\bar{1}\bar{1}1)$ terrace. This means the x-y plane contains the direction $[\bar{2}1\bar{1}]$. Then in the global basis, the coordinates of the edge vectors will be $\vec{L}_1 = (L_x, 0, 0)$, $\vec{L}_2 = (xy, L_y, 0)$ and $\vec{L}_3 = (xz, yz, L_z)$. The following equations can be derived based on trigonometric relations.

$$L_x = L_1 = 63.602 \, \text{Å}$$
$$xy = L_2 \cos \gamma = -0.785 \, \text{Å}$$
$$xz = L_3 \cos \beta = 4.273 \, \text{Å}$$
$$L_y = \left(L_2^2 - xy^2\right)^{1/2} = 81.625 \, \text{Å} \qquad (C.2)$$
$$yz = \frac{(L_2 L_3 \cos \alpha - xy.xz)}{L_y} = -30.763 \, \text{Å}$$
$$L_z = \left(L_3^2 - xz^2 - yz^2\right)^{1/2} = 62.904 \, \text{Å}$$

These parameters allow definition of the simulation box (refer Fig. C.1(i)-(iii)). Next, the crystal must be defined in a specific orientation. The orientation of the crystallographic vectors {[100], [010], [001]} must be specified in the global basis $\{\hat{i}, \hat{j}, \hat{k}\}$. For this purpose, the set of vector equations $\vec{L}_1 = 10[011]$, $\vec{L}_2 = 10[\bar{2}1\bar{1}]$ and $\vec{L}_3 = 10[\bar{1}\bar{1}1]$ can be recast in a matrix form:

$$10 \begin{pmatrix} 0 & 1 & 1 \\ -2 & 1 & -1 \\ -1 & -1 & 1 \end{pmatrix} \begin{pmatrix} [100] \\ [010] \\ [001] \end{pmatrix} = \begin{pmatrix} L_x & 0 & 0 \\ xy & L_y & 0 \\ xz & yz & L_z \end{pmatrix} \begin{pmatrix} \hat{i} \\ \hat{j} \\ \hat{k} \end{pmatrix} \qquad (C.3)$$
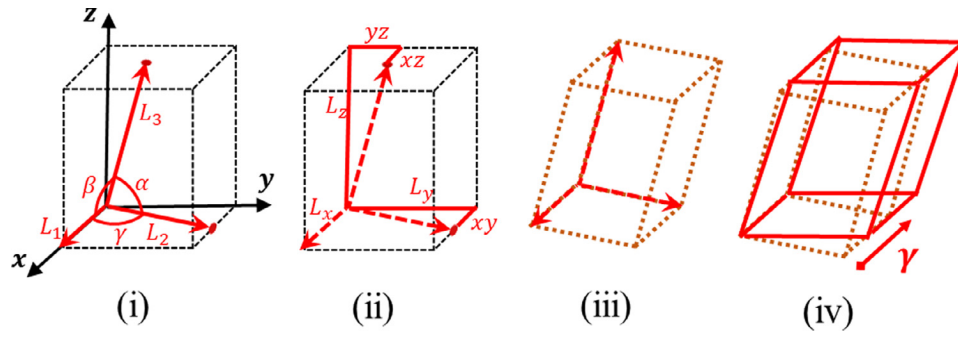
Fig. C.1. Schematic construction of simulation box (i) The edge vectors and angles between them are indicated in the global basis (ii) Components of the edge vectors projected on the global basis are shown (iii) Schematic of strain-free simulation box (iv) In-plane shear applied on the *xy* plane to strain the simulation box.
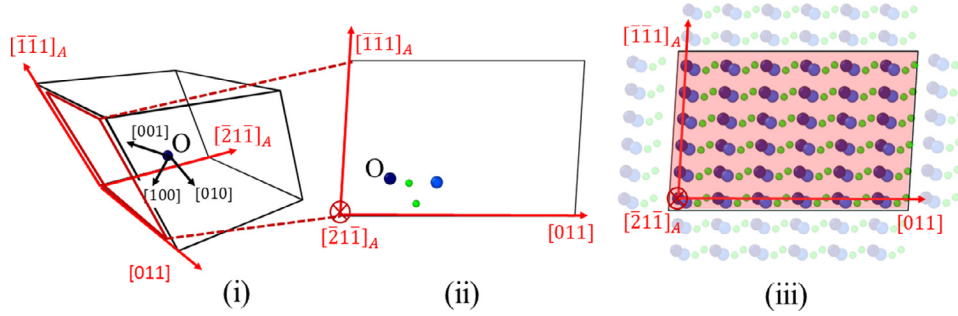

Fig. C.2. Construction of variant A structure in the simulation box; (i) Simulation box with edge vectors aligned with crystallographic directions; a reference lattice Ti site (marked as O) is shown, marked with the oriented unit cell vectors (ii) The {211} projection is shown with the same lattice Ti site and accompanying motif atoms (iii) Variant A is constructed by repeating the motif arrangement at each point of the oriented lattice; the atoms inside the simulation box are retained while the ones outside are ignored (by LAMMPS).

Then, the crystallographic unit cell vectors can be expressed in the global basis as:

$$[100] = -0.116\hat{i} - 1.695\hat{j} - 2.097\hat{k}$$
$$[010] = 3.025\hat{i} + 2.386\hat{j} - 2.097\hat{k} \tag{C.4}$$
$$[001] = 3.336\hat{i} - 2.386\hat{j} - 2.097\hat{k}$$

It can be verified that $|100| = a = 2.699\,\text{Å}$, $|010| = b = 4.386\,\text{Å}$, $|001| = c = 4.606\,\text{Å}$. In this form, the lattice corresponds to unstrained variant A configuration. However, Section 2.1 and Appendix A establishes the need for coherence strains in both variants. The shear deformation to be applied, as indicated in Fig. A.1, can be represented by the deformation gradient:

$$\mathbf{F} = \begin{pmatrix} 1 & \gamma & 0 \\ 0 & 1 & 0 \\ 0 & 0 & 1 \end{pmatrix} \tag{C.5}$$

The deformation gradient is referenced to the global basis. Here, $\gamma = 0.96\%$, which is identical to $-xy/L_y$. This deformation gradient is applied to the entire simulation box. This is done by operating the deformation gradient on the current edge vectors to generate edge vectors for the strained box. Hence, the new edge vectors are:

$$\mathbf{F}\begin{pmatrix} L_x \\ 0 \\ 0 \end{pmatrix} = \begin{pmatrix} L_x \\ 0 \\ 0 \end{pmatrix}; \mathbf{F}\begin{pmatrix} xy \\ L_y \\ 0 \end{pmatrix} = \begin{pmatrix} 0 \\ L_y \\ 0 \end{pmatrix}; \mathbf{F}\begin{pmatrix} xz \\ yz \\ L_z \end{pmatrix} = \begin{pmatrix} xz - \frac{yz}{L_y}.xy \\ yz \\ L_z \end{pmatrix} \tag{C.6}$$

After straining, the edge vector [011] (parallel to the *x*-axis) remains unchanged, but the direction $[\bar{2}1\bar{1}]$ is now parallel to the *y*-axis. To get the crystallographic unit cell vectors corresponding to the strained variant A, we reapply (C.3), except with the modified edge vectors. Hence, we have the matrix of vector equations as

$$10\begin{pmatrix} 0 & 1 & 1 \\ -2 & 1 & -1 \\ -1 & -1 & 1 \end{pmatrix} \begin{pmatrix} [100] \\ [010] \\ [001] \end{pmatrix} = \begin{pmatrix} L_x & 0 & 0 \\ 0 & L_y & 0 \\ xz - \frac{yz}{L_y}.xy & yz & L_z \end{pmatrix} \begin{pmatrix} \hat{i} \\ \hat{j} \\ \hat{k} \end{pmatrix}, \tag{C.7}$$

resulting in:

$$[100] = -0.132\hat{i} - 1.695\hat{j} - 2.097\hat{k}$$
$$[010] = 3.047\hat{i} + 2.386\hat{j} - 2.097\hat{k} \tag{C.8}$$
$$[001] = 3.313\hat{i} - 2.386\hat{j} - 2.097\hat{k}$$

Essentially, the coherence strain translates to applying a certain strain at the unit cell level. The lattice can now be generated. Starting from a reference point, the rest of the lattice points are generated from it using the lattice vectors defined in Equations (C.8). This reference is specified as the "origin", O. The origin essentially represents coordinates of one lattice point in space, in the global basis. Changing the origin by a magnitude smaller than the lattice spacing (in any direction) allows the lattice to physically translate in space. Hence it is alternatively viewed as a specification of lattice shift. If the translation magnitudes in each direction equal lattice spacings of those directions (or their multiples), the lattice remains invariant. Once the lattice is defined in space, the motif arrangement is repeated at each lattice point to complete the crystal definition. Hence, the motif arrangement corresponding to B19′ martensite (taken from [82], illustrated in Fig. 1(i)) is chosen. The atoms that fall within the boundaries of the simulation box are retained while those that are outside are ignored. The definition and straining of the simulation box is schematically shown in Fig. C.1. The construction of the atomic structure in variant A is illustrated in Fig. C.2. Only the projections on the $(\bar{2}1\bar{1})$ plane is shown for simplicity of presentation.
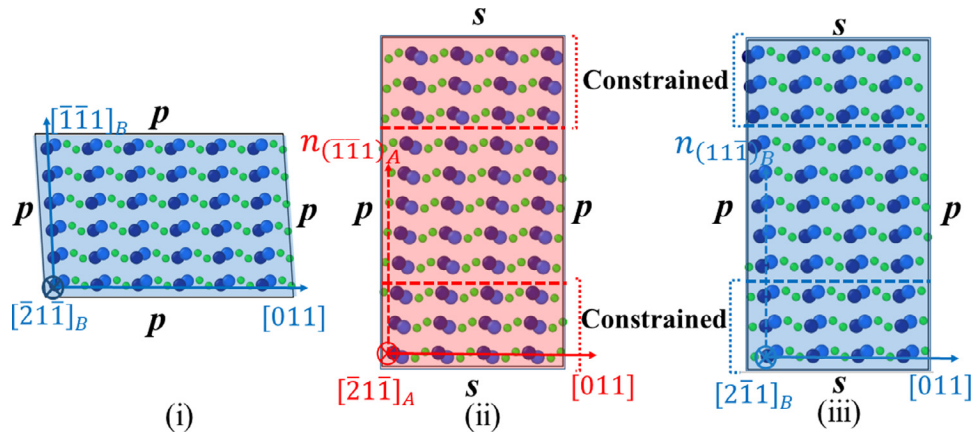
Fig. C.3. (i) Variant B constructed in a simulation with edge vectors along respective crystallographic directions (ii) Variant A structure with the edge vector $\vec{L}_3$ along the normal to the $(\bar{1}\bar{1}1)_A$ plane; periodic boundary conditions (p) can be enforced along the lateral directions [011] and $[\bar{2}1\bar{1}]_A$; shrink-wrapped boundary condition (s) are enforced with a constrained layer in the normal direction (iii) Variant B structure constructed in the same way as (ii).
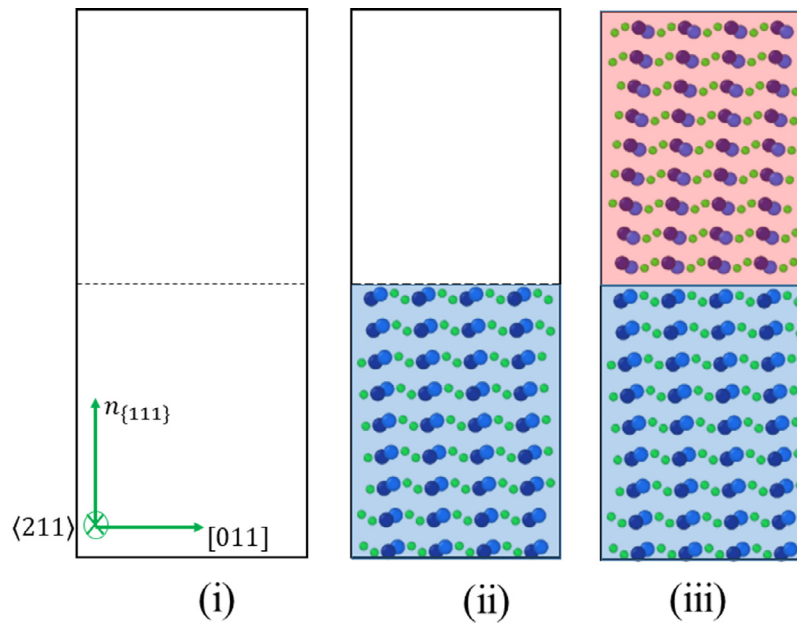

Fig. C.4. (i) Simulation box is defined with two regions (ii) Variant B is defined such that the atomic planes clear the partition with sufficient tolerance (iii) Variant A is constructed in the top region (accurate definition of the structure requires the calculation of lattice offsets, elaborated in Section 2.2).

Repeating this for variant B, we construct the structure in Fig. C.3(i). In both structures (Fig. C.2 (iii) and Fig. C.3), since the edge vectors are crystallographic directions, periodic boundary conditions can be enforced across the parallelepiped faces. This allows a simulation of the bulk material within Molecular Statics (MS). To check the stability of the structure (in variant A or B), the simulation box was relaxed within periodic boundary conditions, until the energy converged within a fractional change of 1.0×10^{-8}. Both structures were stable, as was expected from the work in [82].

However, if the {111} terrace of the Type II twin boundary is to be simulated, then both variants must be constructed within the same simulation box. Then the choice of a suitable edge vector $\vec{L}_3$ is not straightforward. In this model, the choice was made to use $\vec{L}_3 || n_{\{111\}}$, where $n_{\{111\}}$ is used to represent $n_{(\bar{1}\bar{1}1)_A} = n_{(11\bar{1})_B}$. Since this vector is not crystallographic, periodic boundary conditions cannot be enforced. Instead, shrink-wrapped boundary conditions are enforced with a constrained/frozen layer in the top and bottom. All the atoms in this layer are frozen in place and constrained from moving in any direction, during the simulation. This layer is

chosen to have a thickness higher than the cut-off of the interatomic potential ($r_c = 5.2$ Å). Based on this constraint, the frozen layer is chosen to contain three {111} planes (with interplanar spacing $d = 2.097$ Å) at both extremities of the z-edge. This constrains the boundary from relaxing as a free-surface and provides a stable structure (representative of the bulk material) for relaxing the atoms within the simulation box. This structure is relaxed with lateral periodic boundary conditions (along x and y), and shrink-wrapped condition along z (as specified before). Both variant structures were found to be stable, and are shown in Fig. C.3(ii) and (iii). Again, only the {211} projections are shown for clarity of presentation. Results from simulation of a smaller simulation box are shown for illustration purposes. The box sizes used for simulations, for instance in Section 2.2, are larger.

Two blocks of variant A and B were constructed in this manner and analyzed for Section 2.1 and Appendix B. They were positioned on top of each other to show that the atomic arrangements in their respective {111} planes are incompatible. This was done to establish the absence of a crystallographic TB between the variants.
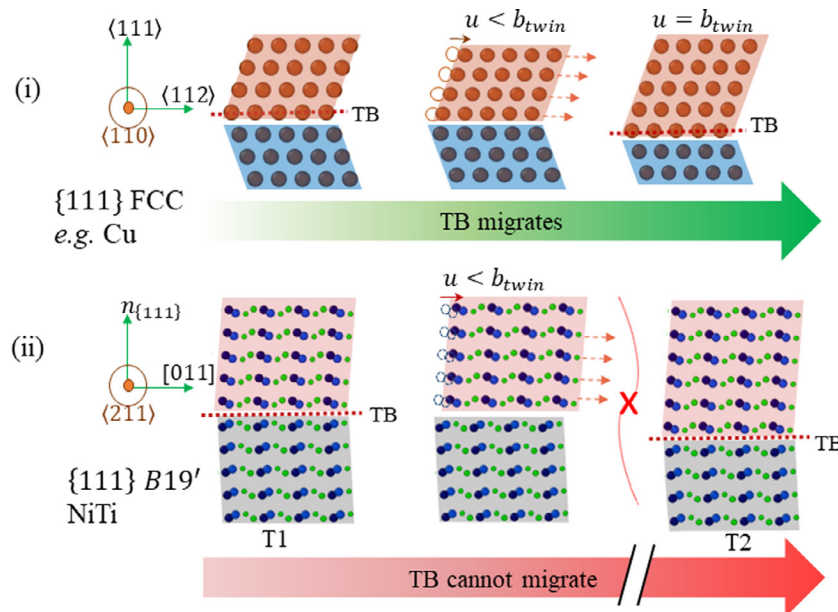
Fig. D.1. A comparative illustration of the validity of enforced rigid displacements to calculate the GPFE twin migration segment in (i) higher symmetry FCC system versus (ii) lower symmetry $B19'$ (TB: Twin Boundary), illustrating the inability of a translation sans shuffle in migrating the TB in $B19'$ martensite.

To construct the twinned structure (the {111} terrace structure) within the simulation box, the following procedure is adopted. The simulation box is partitioned into two regions. The strained structure of variant B is filled in the bottom region. We establish in Section 2.2 and Appendix B that the twin boundary cannot be an atomic plane and can only exist as a virtual boundary separating the variants. Hence, the origin of variant B is chosen such that the first atomic plane nearest to the partition clears it with sufficient tolerance. Now variant A is constructed in the top region. The distance between the origins defines the offsets. The definition and calculation of lattice offsets is elaborated in Section 2.2.

Appendix D. GPFE: Key differences from higher-symmetry crystallographic structures

Although the procedure to calculate the GSFE/GPFE is fairly standard [79] and finds ubiquitous presence in understanding twinning energy barriers [31–33] it shall be briefly repeated here. This repetition is necessary to elaborate the intricacies that separate twinning in high-symmetry BCC/FCC systems from the low-symmetry phase dealt with here. In these cubic phases, the twinning mode is *only* of the compound type [87]. To extract the twin migration part of the GPFE, we need to setup a TB with two variant blocks in a relaxed state. Then, keeping one part of the configuration fixed rigidly, the remaining part is rigidly translated over it and the energy is extracted at each incremented position. In other words, a translational disregistry is introduced and the associated energy cost obtained per unit area. In the example shown in Fig. D.1(i), the translated part consists of the top twin variant along with the crystallographic TB. Atomic shuffles normal to the twinning plane are allowed while those along the direction of translation are ignored. As the translation occurs, the top part crosses the unstable twinning energy and then forms an additional twinned plane, with the crystallographic TB having moved down by one plane. The example is based on twinning in a high-symmetry cubic phase, FCC Cu on the {111} plane [95].

Now, attempt the same procedure with the $B19'$ TB setup. The initial twin configuration T1 is shown in Fig. D.1(ii). The rigidly translated part includes the top variant M_A. The net displacement that must be achieved at the top boundary with respect to the bottom fixed boundary should equal the twinning partial magnitude. The initial and final states are already known from the previous analysis of crystallography (Section 2.3), and the objective is to get to configuration T2 from T1. A reliable estimate of the twinning partial is available from [20] and is *approximately* 1/9 [011]. If a translation of this magnitude is enforced without allowing any shuffles parallel to the direction of translation, then the resulting structure would not resemble that of T2. Hence, there is a need to allow shuffles parallel to the direction of shear/translation. This is implemented in the procedure outlined in Section 2.4, where the rigid displacements are only applied to specific atomic sites (lattice Ti only) while the remaining (motif Ti and Ni atoms) are allowed to shuffle.

Supplementary materials

Supplementary material associated with this article can be found, in the online version, at doi:10.1016/j.actamat.2019.10.048.

References

[1] M. Bönisch, Y. Wu, H. Sehitoglu, Twinning-induced strain hardening in dual-phase FeCoCrNiAl0.5 at room and cryogenic temperature, Sci. Rep. 8 (1) (2018) 10663.

[2] S. Alkan, P. Chowdhury, H. Sehitoglu, R.G. Rateick, H.J. Maier, Role of nanotwins on fatigue crack growth resistance – Experiments and theory, Int. J. Fatigue 84 (2016) 28–39.

[3] L. Rémy, The interaction between slip and twinning systems and the influence of twinning on the mechanical behavior of FCC metals and alloys, Metall. Trans. A 12 (3) (1981) 387–408.

[4] C.N. Reid, A review of mechanical twinning in body-centred cubic metals and its relation to brittle fracture, J. Less Common Met. 9 (2) (1965) 105–122.

[5] S. Mahajan, D.F. Williams, Deformation twinning in metals and alloys, Int. Metall. Rev. 18 (2) (1973) 43–61.

[6] J.W. Christian, S. Mahajan, Deformation twinning, Prog. Mater. Sci. 39 (1) (1995) 1–157.

[7] T. Ezaz, H. Sehitoglu, W. Abuzaid, H.J. Maier, Higher order twin modes in martensitic NiTi—the (201⁻) case, Mater. Sci. Eng. A 558 (2012) 422–430.

[8] J.X. Zhang, M. Sato, A. Ishida, Deformation mechanism of martensite in Ti-rich Ti–Ni shape memory alloy thin films, Acta Mater. 54 (4) (2006) 1185–1198.

[9] N. Zárubová, Y. Ge, O. Heczko, S.P. Hannula, In situ tem study of deformation twinning in Ni–Mn–Ga non-modulated martensite, Acta Mater. 61 (14) (2013) 5290–5299.

[10] J.M. Young, K.J. Van Vliet, Predicting in vivo failure of pseudoelastic NiTi devices under low cycle, high amplitude fatigue, J. Biomed. Mater. Res. Part B 72B (1) (2005) 17–26.

[11] S. Miyazaki, K. Otsuka, C.M. Wayman, The shape memory mechanism associated with the martensitic transformation in Ti·Ni alloys—II. Variant coalescence and shape recovery, Acta Metall. 37 (7) (1989) 1885–1890.

[12] S. Miyazaki, K. Otsuka, C.M. Wayman, The shape memory mechanism associated with the martensitic transformation in Ti·Ni alloys—I. Self-accommodation, Acta Metall. 37 (7) (1989) 1873–1884.

[13] Y. Liu, Z. Xie, J.V. Humbeeck, L. Delaey, Y. Liu, On the deformation of the twinned domain in NiTi shape memory alloys, Philos. Mag. A 80 (8) (2000) 1935–1953.

[14] Y. Liu, Z.L. Xie, J. Van Humbeeck, L. Delaey, Effect of texture orientation on the martensite deformation of NiTi shape memory alloy sheet, Acta Mater. 47 (2) (1999) 645–660.

[15] T. Duerig, A. Pelton, D. Stöckel, An overview of nitinol medical applications, Mater. Sci. Eng. A 273-275 (1999) 149–160.

[16] K. Otsuka, X. Ren, Physical metallurgy of Ti–Ni-based shape memory alloys, Prog. Mater. Sci. 50 (2005) 511–678.

[17] T. Onda, Y. Bando, T. Ohba, K. Otsuka, Electron microscopy study of twins in martensite in a Ti-50.0 at%Ni alloy, Mater. Tran. JIM 33 (4) (1992) 354–359.

[18] M. Nishida, H. Ohgi, I. Itai, A. Chiba, K. Yamauchi, Electron microscopy studies of twin morphologies in B19′ martensite in the Ti-Ni shape memory alloy, Acta Metall. Mater. 43 (3) (1995) 1219–1227.

[19] Y. Liu, Z.L. Xie, The rational nature of type II twin in NiTi shape memory alloy, J. Intell. Mater. Syst. Struct. 17 (12) (2006) 1083–1090.

[20] T. Ezaz, H. Sehitoglu, Type ii detwinning in NiTi, Appl. Phys. Lett. 98 (14) (2011) 141906.

[21] Z.L. Xie, Y. Liu, HRTEM study of ⟨011⟩ type II twin in NiTi shape memory alloy, Philos. Mag. 84 (32) (2004) 3497–3507.

[22] K.M. Knowles, D.A. Smith, The crystallography of the martensitic transformation in equiatomic nickel-titanium, Acta Metall. 29 (1) (1981) 101–110.

[23] B.A. Bilby, A.G. Crocker, The theory of the crystallography of deformation twinning, Proc. R. Soc. Lond. Ser. A. Math. Phys. Sci. 288 (1413) (1965) 240–255.

[24] H. Tobe, H.Y. Kim, T. Inamura, H. Hosoda, S. Miyazaki, Origin of {332} twinning in metastable β-Ti alloys, Acta Mater. 64 (2014) 345–355.

[25] C. Cayron, Shifting the shear paradigm in the crystallographic models of displacive transformations in metals and alloys, Crystals 8 (4) (2018).

[26] X. Ji, I. Gutierrez-Urrutia, S. Emura, T. Liu, T. Hara, X. Min, D. Ping, K. Tsuchiya, Twinning behavior of orthorhombic-α″ martensite in a Ti-7.5Mo alloy, Sci. Technol. Adv. Mater. 20(1) (2019) 401–411.

[27] D.S. Lieberman, M.S. Wechsler, T.A. Read, Cubic to orthorhombic diffusionless phase change— experimental and theoretical studies of AuCd, J. Appl. Phys. 26 (4) (1955) 473–484.

[28] C.M. Wayman, The phenomenological theory of martensite crystallography: interrelationships, Metall. Mat. Trans. A 25 (9) (1994) 1787–1795.

[29] R.D. James, K.F. Hane, Martensitic transformations and shape-memory materials, Acta Mater. 48 (1) (2000) 197–222.

[30] E. Patoor, D.C. Lagoudas, P.B. Entchev, L.C. Brinson, X Gao, Shape memory alloys, part I: general properties and modeling of single crystals, Mech. Mater. 38 (5) (2006) 391–429.

[31] P. Chowdhury, H. Sehitoglu, Atomistic energetics and critical twinning stress prediction in face and body centered cubic metals: recent progress, J. Eng. Mater. Technol. 140 (2) (2018) 020801–020801-19.

[32] A. Ojha, H. Sehitoglu, Critical stresses for twinning, slip, and transformation in Ti-based shape memory alloys, Shape Mem. Superelasticity 2 (2) (2016) 180–195.

[33] J. Wang, H. Sehitoglu, Twinning stress in shape memory alloys: theory and experiments, Acta Mater. 61 (18) (2013) 6790–6801.

[34] Y.H. Zhao, Y.T. Zhu, X.Z. Liao, Z. Horita, T.G. Langdon, Tailoring stacking fault energy for high ductility and high strength in ultrafine grained cu and its alloy, Appl. Phys. Lett. 89 (12) (2006) 121906.

[35] C. Maletta, E. Sgambitterra, F. Furgiuele, R. Casati, A. Tuissi, Fatigue properties of a pseudoelastic niti alloy: strain ratcheting and hysteresis under cyclic tensile loading, Int. J. Fatigue 66 (2014) 78–85.

[36] W. Abuzaid, H. Sehitoglu, Functional fatigue of Ni50.3Ti25Hf24.7 – Heterogeneities and evolution of local transformation strains, Mater. Sci. Eng. A 696 (2017) 482–492.

[37] W. Abuzaid, H. Sehitoglu, Superelasticity and functional fatigue of single crystalline FeNiCoAlTi iron-based shape memory alloy, Mater. Des. 160 (2018) 642–651.

[38] G. Eggeler, E. Hornbogen, A. Yawny, A. Heckmann, M. Wagner, Structural and functional fatigue of niti shape memory alloys, Mater. Sci. Eng. A 378 (1) (2004) 24–33.

[39] D.M. Norfleet, P.M. Sarosi, S. Manchiraju, M.F.X. Wagner, M.D. Uchic, P.M. Anderson, M.J. Mills, Transformation-induced plasticity during pseudoelastic deformation in Ni–Ti microcrystals, Acta Mater. 57 (12) (2009) 3549–3561.

[40] T. Simon, A. Kröger, C. Somsen, A. Dlouhy, G. Eggeler, On the multiplication of dislocations during martensitic transformations in NiTi shape memory alloys, Acta Mater. 58 (5) (2010) 1850–1860.

[41] S. Kajiwara, W.S. Owen, Substructure of austenite formed by a partial reverse martensitic transformation in an Fe-Pt alloy, Metall. Trans. 4 (8) (1973) 1988–1990.

[42] S. Kajiwara, T. Kikuchi, Dislocation structures produced by reverse martensitic transformation in a Cu-Zn alloy, Acta Metall. 30 (2) (1982) 589–598.

[43] N. Zou, Z. Li, Y. Zhang, B. Yang, X. Zhao, C. Esling, L. Zuo, Plastic deformation of Ni–Mn-Ga 7M modulated martensite by twinning & detwinning and inter-martensitic transformation, Int. J. Plast. 100 (2018) 1–13.

[44] O. Heczko, Understanding motion of twin boundary—A key to magnetic shape memory effect, IEEE Trans. Magn. 50 (11) (2014) 1–7.

[45] T. Hara, T. Ohba, S. Miyazaki, K. Otsuka, Electron microscopy study of type II twins in γ′₁ Cu-Al-Ni martensite, materials transactions, JIM 33 (12) (1992) 1105–1113.

[46] D.Z. Liu, D. Dunne, Atomic force microscope study of the interface of twinned martensite in copper–aluminium–nickel, Scr. Mater. 48 (12) (2003) 1611–1616.

[47] K. Okamoto, S. Ichinose, K. Morii, K. Otsuka, K. Shimizu, Crystallography of β1 → γ′1 stress-induced martensitic transformation in a Cu-Al-Ni alloy, Acta Metall. 34 (10) (1986) 2065–2073.

[48] K. Adachi, J. Perkins, C.M. Wayman, Type ii twins in self-accommodating martensite plate variants in a Cu-Zn-Al shape memory alloy, Acta Metall. 34 (12) (1986) 2471–2485.

[49] K. Morii, T. Ohba, K. Otsuka, H. Sakamoto, K. Shimizu, Crystallography of β2 → γ2′ martensitic transformation in au-47.5 at.% cd and au-47.5 at.% Cd-Cu alloys, Acta Metall. Mater. 39 (11) (1991) 2719–2725.

[50] K.M. Knowles, A high-resolution electron microscope study of nickel-titanium martensite, Philos. Mag. A 45 (3) (1982) 357–370.

[51] J.W. Christian, CHAPTER 20 - Deformation Twinning, in: J.W. Christian (Ed.), The Theory of Transformations in Metals and Alloys, Pergamon, Oxford, 2002, pp. 859–960.

[52] Y. Liu, Z.L. Xie, Twinning and detwinning of ⟨011⟩ type II twin in shape memory alloy, Acta Mater. 51 (18) (2003) 5529–5543.

[53] H. Zhang, C. Zhang, Y. Zhang, X. Wang, C. Esling, X. Zhao, L. Zuo, Crystallographic insights into Ni-Co-Mn-in metamagnetic shape memory alloys, J. Appl. Cryst. 49 (5) (2016) 1585–1592.

[54] M. Nishida, K. Yamauchi, I. Itai, H. Ohgi, A. Chiba, High resolution electron microscopy studies of twin boundary structures in B19′ martensite in the Ti-Ni shape memory alloy, Acta Metall. Mater. 43 (3) (1995) 1229–1234.

[55] M. Nishida, T. Hara, M. Matsuda, S. Ii, Crystallography and morphology of various interfaces in Ti–Ni, Ti–Pd and Ni–Mn–Ga shape memory alloys, Mater. Sci. Eng. A 481-482 (2008) 18–27.

[56] M. Matsuda, Y. Yasumoto, K. Hashimoto, T. Hara, M. Nishida, Transmission electron microscopy of twins in 10M Martensite in Ni-Mn-Ga ferromagnetic shape memory alloy, Mater. Trans. (2012) 1203191599-1203191599.

[57] J.P. Hirth, R.C. Pond, Steps, dislocations and disconnections as interface defects relating to structure and phase transformations, Acta Mater. 44 (12) (1996) 4749–4763.

[58] R.C. Pond, X. Ma, Y.W. Chai, J.P. Hirth, Chapter 74 topological modelling of martensitic transformations, in: F.R.N. Nabarro, J.P. Hirth (Eds.), Dislocations in Solids, Elsevier, 2007, pp. 225–261.

[59] J.P. Hirth, J. Wang, C.N. Tomé, Disconnections and other defects associated with twin interfaces, Prog. Mater. Sci. 83 (2016) 417–471.

[60] R.C. Pond, J.P. Hirth, Defects at surfaces and interfaces, in: H. Ehrenreich, D. Turnbull (Eds.), Solid State Physics, Academic Press, 1994, pp. 287–365.

[61] G.B. Olson, M. Cohen, Interphase-boundary dislocations and the concept of coherency, Acta Metall. 27 (12) (1979) 1907–1918.

[62] F.C. Frank, J.H. van der Merwe, F. Mott Nevill, One-dimensional dislocations. I. Static theory, Proc. R. Soc. Lond. Ser. A. Math. Phys. Sci. 198 (1053) (1949) 205–216.

[63] J.W. Christian, Crystallographic theories, interface structures, and transformation mechanisms, Metall. Mater. Trans. A 25 (9) (1994) 1821–1839.

[64] R.C. Pond, X. Ma, J.P. Hirth, T.E. Mitchell, Disconnections in simple and complex structures, Philos. Mag. 87 (33) (2007) 5289–5307.

[65] J.M. Howe, R.C. Pond, J.P. Hirth, The role of disconnections in phase transformations, Prog. Mater. Sci. 54 (6) (2009) 792–838.

[66] R.C. Pond, S. Celotto, J.P. Hirth, A comparison of the phenomenological theory of martensitic transformations with a model based on interfacial defects, Acta Mater. 51 (18) (2003) 5385–5398.

[67] X. Ma, R.C. Pond, Parent–martensite interface structure in ferrous systems, J. Nucl. Mater. 361 (2) (2007) 313–321.

[68] X. Ma, R.C. Pond, Martensitic interfaces and transformation crystallography in Pu–Ga alloys, J. Mater. Sci. 46 (12) (2011) 4236–4242.

[69] J.S. Bowles, J.K. Mackenzie, The crystallography of martensite transformations I, Acta Metall. 2 (1) (1954) 129–137.

[70] R.C. Pond, J.P. Hirth, Topological model of type II deformation twinning, Acta Mater. 151 (2018) 229–242.

[71] R.C. Pond, J.P. Hirth, K.M. Knowles, Topological model of type II deformation twinning in NiTi martensite, Philos. Mag. 99 (13) (2019) 1619–1632.

[72] I.J. Beyerlein, X. Zhang, A. Misra, Growth twins and deformation twins in metals, Annu. Rev. Mater. Res. 44 (1) (2014) 329–363.

[73] R.C. Pond, J.P. Hirth, A. Serra, D.J. Bacon, Atomic displacements accompanying deformation twinning: shears and shuffles, Mater. Res. Lett. 4 (4) (2016) 185–190.

[74] S. Dilibal, Investigation of nucleation and growth of detwinning mechanism in martensitic single crystal NiTi using digital image correlation, Metallogr. Microstruct. Anal. 2 (4) (2013) 242–248.

[75] J. Wang, H. Sehitoglu, Martensite modulus dilemma in monoclinic NiTi-theory and experiments, Int. J. Plast. 61 (2014) 17–31.

[76] S. Plimpton, Fast parallel algorithms for short-range molecular dynamics, J. Comput. Phys. 117 (1) (1995) 1–19.

[77] J. Hafner, Ab-initio simulations of materials using VASP: density-functional theory and beyond, J. Comput. Chem. 29 (13) (2008) 2044–2078.

[78] B. Li, K.M. Knowles, Molecular dynamics simulation of twinning in devitrite, Na2Ca3Si6O16, Philos. Mag. 93 (13) (2013) 1582–1603.

[79] S. Ogata, J. Li, S. Yip, Energy landscape of deformation twinning in bcc and FCC metals, Phys. Rev. B 71 (22) (2005) 224102.

[80] W.-S. Ko, B. Grabowski, J. Neugebauer, Development and application of a Ni-Ti interatomic potential with high predictive accuracy of the martensitic phase transition, Phys. Rev. B 92 (13) (2015) 134107.

[81] Y. Zhong, K. Gall, T. Zhu, Atomistic study of nanotwins in NiTi shape memory alloys, J. Appl. Phys. 110 (3) (2011) 033532.

[82] G. Ren, H. Sehitoglu, Interatomic potential for the NiTi alloy and its application, Comput. Mater. Sci. 123 (2016) 19–25.

[83] Y. Kudoh, M. Tokonami, S. Miyazaki, K. Otsuka, Crystal structure of the martensite in Ti-49.2 at.%Ni alloy analyzed by the single crystal X-ray diffraction method, Acta Metall. 33 (11) (1985) 2049–2056.

[84] N. Hatcher, O.Y. Kontsevoi, A.J. Freeman, Role of elastic and shear stabilities in the martensitic transformation path of NiTi, Phys. Rev. B 80 (14) (2009) 144203.

[85] K. Otsuka, T. Sawamura, K. Shimizu, Crystal structure and internal defects of equiatomic tini martensite, Phys. Status Solidi (a) 5 (2) (1971) 457–470.

[86] A.J. Vattré, M.J. Demkowicz, Partitioning of elastic distortions at a semicoherent heterophase interface between anisotropic crystals, Acta Mater. 82 (2015) 234–243.

[87] A. Kelly, K.M. Knowles, in: Chapter 11 - Twinning, Crystallography and Crystal Defects, John Wiley & Sons Ltd., Chichester, UK, 2012, pp. 335–361.

[88] P.D. Bristowe, A.G. Crocker, A computer simulation study of the structures of twin boundaries in body-centred cubic crystals, Philos. Mag. J. Theor. Exp. Appl. Phys. 31 (3) (1975) 503–517.

[89] R. Schweinfest, F. Ernst, T. Wagner, M. Rühle, High-precision assessment of interface lattice offset by quantitative HRTEM, J. Microsc. 194 (1) (1999) 142–151.

[90] M.D. Sangid, H. Sehitoglu, H.J. Maier, T. Niendorf, Grain boundary characterization and energetics of superalloys, Mater. Sci. Eng. A 527 (26) (2010) 7115–7125.

[91] V. Vítek, Multilayer stacking faults and twins on {211} planes in B.C.C. metals, Scr. Metall. 4 (9) (1970) 725–732.

[92] A. Ojha, H. Sehitoglu, L. Patriarca, H.J. Maier, Twin nucleation in Fe-based bcc alloys—modeling and experiments, Model. Simul. Mater. Sci. Eng. 22 (7) (2014) 075010.

[93] R.C. Pond, D.L. Medlin, A. Serra, A study of the accommodation of coherency strain by interfacial defects at a grain boundary in gold, Philos. Mag. 86 (29–31) (2006) 4667–4684.

[94] B. Li, K.M. Knowles, Molecular dynamics simulation of albite twinning and pericline twinning in low albite, Model. Simul. Mater. Sci. Eng. 21 (5) (2013) 055012.

[95] S. Kibey, J.B. Liu, D.D. Johnson, H. Sehitoglu, Generalized planar fault energies and twinning in Cu–Al alloys, Appl. Phys. Lett. 89 (19) (2006) 191911.